The Thesis Committee for Abhishek Dilip Bihani
Certifies that this is the approved version of the following thesis:

Pore Size Distribution and Methane Equilibrium Conditions at Walker Ridge Block 313, Northern Gulf of Mexico

APPROVED BY
SUPERVISING COMMITTEE:

Supervisor:

Hugh Daigle

Ryosuke Okuno

Pore Size Distribution and Methane Equilibrium Conditions at Walker Ridge Block 313, Northern Gulf of Mexico

by

Abhishek Dilip Bihani, B.E.

Thesis

Presented to the Faculty of the Graduate School of

The University of Texas at Austin

in Partial Fulfillment

of the Requirements

for the Degree of

Master of Science in Engineering

The University of Texas at Austin

May 2016

Dedication

To my parents, Dilip and Hema, and my brother, Anurag who always believed in me.

Acknowledgements

My academic experience in graduate studies from the University of Texas at Austin has been highly rewarding and fulfilling, and I wish to thank everyone who made it possible. Foremost, I would like to express my deepest gratitude to my graduate supervisor, Dr. Hugh Daigle for his inspiration, patience, unwavering support and guidance throughout this project. My profound thanks to Dr. Ryosuke Okuno for taking the time to review my thesis and for his valuable feedback.

I would like to express my sincere appreciation to the U.S. Department of Energy for funding this project. This study has been conducted as a part of the DOE Project: 'Mechanisms for methane transport and hydrate accumulation in coarse-grained reservoirs' (US DOE Award DE-FE0013919).

I would like to acknowledge Deborah Glosser and Dr. Ann Cook of Ohio State University for conducting the MICP tests used in this work. I am also grateful to Dr. Xiaoli Liu, Dr. Peter Flemings and Dr. Kehua You for their assistance in conducting the thermodynamic calculations.

My utmost gratitude to Frankie Hart, Leilani Swafford and Amy Stewart for the administrative help during my studies here at the University of Texas at Austin. I also wish to thank the other members of the methane hydrates group; Michael, Ryan and Arash for the fruitful discussions during my research and my friends in and around Austin; Ashwin D., Shivam, Neha, Sanika, Satyajit, Ashwin P., Tejas, Abhijeet, Chaitanya and Aman for their moral support.

Finally, I would like to thank my family in India and U.S.A. for keeping me motivated and strong towards fulfilling my goal of obtaining a graduate degree at the University of Texas at Austin.

Abstract

Pore Size Distribution and Methane Equilibrium Conditions at Walker Ridge Block 313, Northern Gulf of Mexico

Abhishek Dilip Bihani, M.S.E.

The University of Texas at Austin, 2016

Supervisor: Hugh Daigle

In-situ pressure, temperature, salinity and pore size may allow coexistence of three methane phases: liquid (L), gas (G), hydrate (H) in marine gas hydrate systems. A discrete zone of three-phase equilibrium may occur near the base of the gas hydrate stability zone (GHSZ) in sediments with salinity close to seawater due to capillary effects. The existence of a three-phase zone affects the location of the bottom-simulating reflection (BSR) and also has repercussions for methane fluxes at the base of the GHSZ.

This project studied the hydrate stability conditions in two wells, WR313-G and WR313-H, at Walker Ridge Block 313 in the northern Gulf of Mexico. The pore size distributions were determined by constructing a synthetic nuclear magnetic resonance (NMR) relaxation time distribution. Correlations were obtained by non-linear regression on NMR, gamma ray, and bulk density logs from well KC-151 at Keathley Canyon. The correlations enabled construction of relaxation time distributions for WR313-G and WR313-H, which were used to predict pore size distribution through comparison with mercury injection capillary pressure measurements.

With the computed pore size distribution, L+H and L+G methane solubility was determined from in-situ pressure and temperature. The intersection of the L+G and L+H curves for various pore sizes allowed calculation of the depth range of the three-phase equilibrium zone. In previous studies at Blake Ridge and Hydrate Ridge, the top of the three-phase zone moves upwards with increasing water depth and overlies the bulk three-phase equilibrium depth but this was not observed at Walker Ridge. In clays at Walker Ridge, the predicted thickness of the three-phase zone is approximately 5 m, but in coarse sands it is only a few centimeters due to the difference in absolute pore sizes and the width of the pore size distribution.

The thick three-phase zone in the clays may explain in part why the BSR is only observed in the sand layers at Walker Ridge, although other factors may influence the presence or absence of a BSR.

Table of Contents

List of Tables

List of Figures

Chapter 1: Introduction

1.1 Research motivation and objectives:

This work particularly studies the hydrate stability conditions in two wells, WR313-G and WR313-H, at Walker Ridge Block 313 in the northern Gulf of Mexico. Coexistence of three methane phases: liquid (L), gas (G), hydrate (H); in marine gas hydrate systems may occur according to in-situ pressure, temperature, salinity and pore size. In sediments with salinity close to seawater, a discrete zone of three-phase equilibrium may occur near the base of the gas hydrate stability zone (GHSZ) due to capillary effects. The existence of a three-phase zone influences the location of the bottom-simulating reflection (BSR) and has implications for methane fluxes at the base of the GHSZ.

The objectives of this research are:

i) To estimate the pore size distributions at Walker Ridge for both clay as well as sand sediments using correlations made with boreholes drilled at Keathley Canyon in the northern Gulf of Mexico based on log data and mercury injection porosimetry data.

ii) To analyze methane stability conditions by investigating the presence of a three-phase zone in both clay and sand sediment types and, if a three-phase zone is present, to determine its depth, thickness and study the effect on BSR interpretation.

1.2 Thesis roadmap:

This thesis aims to shed light on the methane stability conditions at Walker Ridge by utilizing pore size distributions and thermodynamically modeling the phase equilibrium and capillary effects of methane in sand and clay sediments.

Chapter 2 has detailed information about the evolution of hydrate studies, chemistry of methane hydrates and basics of hydrate stability conditions. It also explains the distribution of marine hydrate resources throughout the world and in Gulf of Mexico.

Chapter 3 predicts the distribution of pore sizes at Walker Ridge from synthetic logs by regression analysis and mercury injection porosimetry data obtained at the Keathley Canyon site. It also give details about location and stratigraphy of Keathley

Canyon and Walker Ridge in addition to explanation about the conversion of relaxation time distributions to pore size distributions.

Chapter 4 contains detailed thermodynamic calculations to study the presence of the three-phase zone in both sand and clay. The calculations take into account the capillary effects in both sediment types.

Chapter 5 discusses the results of the calculations and compares the three-phase zone to the one found at Blake Ridge on the U.S. Atlantic Margin. It also examines the potential implications of the existence of a three-phase zone on the BSR. Finally, it discusses the assumptions made in the calculations and the future work that is planned at Walker Ridge 313.

Chapter 6 discusses the implications of this work, the further research planned as a consequence of this project and the conclusion.

Chapter 2: Background

Gas hydrates are solid, ice-like compounds of water and naturally occurring gases such as methane that are stable under conditions of high pressure, low temperature, as well as sufficient gas abundance, water activity and pore sizes (Lee and Collett, 2008; Malinverno, 2010; Ruppel et al., 2008). They represent a presently untapped massive energy resource containing most of the world's methane, about 10^5 trillion standard cubic feet according to Boswell and Collett (2006). Water molecules make up about 85 mol % of gas hydrate as a crystalline lattice (Sloan and Koh, 2007). The lattice is stabilized by guest molecules such as methane that are enclosed in the lattice cavities. Sloan and Koh (2007) also state that while for stability, at least 70% of the cavities need to be occupied by methane, usually the number exceeds 95%. The stability conditions for naturally occurring hydrates are fulfilled in the shallow subsurface of deepwater continental margins and sediments below terrestrial permafrost in polar regions. Hydrates are a highly concentrated source of methane with a cubic meter of hydrate containing as much as 0.8 m^3 of water and more than 160 m^3 methane at standard temperature-pressure conditions. While ethane, propane and carbon dioxide also form gas hydrates, on a global scale methane hydrates are the most dominant ones formed in nature (Ruppel, 2011).

Figure 2.1: Burning gas hydrate (Pinkston and Stern, 2010)

Many drilling and evaluation studies conducted in recent times have indicated that hydrates occur in abundance in marine settings with about only 1% of global gas hydrates occurring in permafrost environments (Ruppel, 2011). Some estimates have gone as far as to predict that hydrocarbon volumes trapped in hydrates may equal the total equivalent energy resources bound in other conventional hydrocarbon sources such as coal, natural gas and oil (Beaudoin et al., 2014). Continuing advances in hydrate related knowledge over the past few decades point towards possibility of large-scale production of gas from hydrates in the coming years which will significantly affect the global energy balance.

2.1 HISTORY OF HYDRATES:

Gas hydrates were first produced in the laboratory in 1810 by the English chemist Sir Humphrey Davy by combining water and chlorine gas to produce a solid (Sloan and Koh, 2007). Thereafter, hydrates were merely regarded as an academic curiosity due to lack of practical applications until the early 20^{th} century.

Gas hydrate plugging became a hindrance with increasing use of pipelines for transporting natural gas by 1930s. Investigations by Hammerschmidt (1934) revealed that despite resemblance to ice, the plugs had a different chemical structure. This led to a wider interest in gas hydrates in order to predict and prevent their formation. This interest further continued into naturally occurring hydrates found during hydrocarbon exploration.

In 1950s, x-ray diffraction studies by von Stackelberg (1954) and others led to confirmation of the clathrate structure of gas hydrates which has guest molecules inside a host lattice but no fixed chemical composition as well as classification of two separate hydrate crystal structures (sI and sII). According to Davidson (1973), this allowed gas hydrate properties to be predicted according to thermodynamic and clathrate models. The third hydrate structure (sH) was discovered in 1987 (Ripmeester, 1987).

Many Russian scientists successfully predicted the stability conditions of pressure and temperature necessary for hydrates to naturally occur are possible in permafrost regions or marine sediments (Sloan and Koh, 2007). Hydrate existence in Arctic

permafrost was established by drilling in 1970s (Davidson et al., 1978). In marine environments, the Deep Sea Drilling Project (DSDP) investigated the anomalous acoustic impedances i.e. bottom-simulating reflectors in the Blake Ridge in the year 1970 (Hollister et al., 1972). Evidences from high gas concentrations in samples prompted further investigation and presence of hydrates was confirmed at Blake Ridge in 1980 in a second expedition (Kvenvolden and Barnard, 1983).

Subsequently drilling campaigns were undertaken in other marine settings like Mackenzie Delta, Hydrate Ridge, Keathley Canyon, Walker Ridge and the results suggest that gas hydrates are present in a wide variety of geological environments such as continental-margins and slope sediments (Bily and Dick, 1974; Milkov et al., 2003; Cook et al., 2008; Boswell et al., 2012).

Hydrates were drilled in the Nankai Trough in Japan for resource assessment including coring and seismic work under the aegis of the Ministry of Economy, Trade and Industry (METI) as a sponsored project in 1999-2000. The energy potential evaluated has led to further investments by Japan in methane hydrates leading to world's first gas production trial from a marine gas-hydrate deposit in the area (Yamamoto, 2015).

According to Collett et al., (2008), the Indian National Gas Hydrate Program (NGHP) expedition was undertaken in 2006 and around 500 cores recovered were studied by a number of research laboratories to give encouraging results.

The timeline of hydrate studies is shown in Figure 2.2.

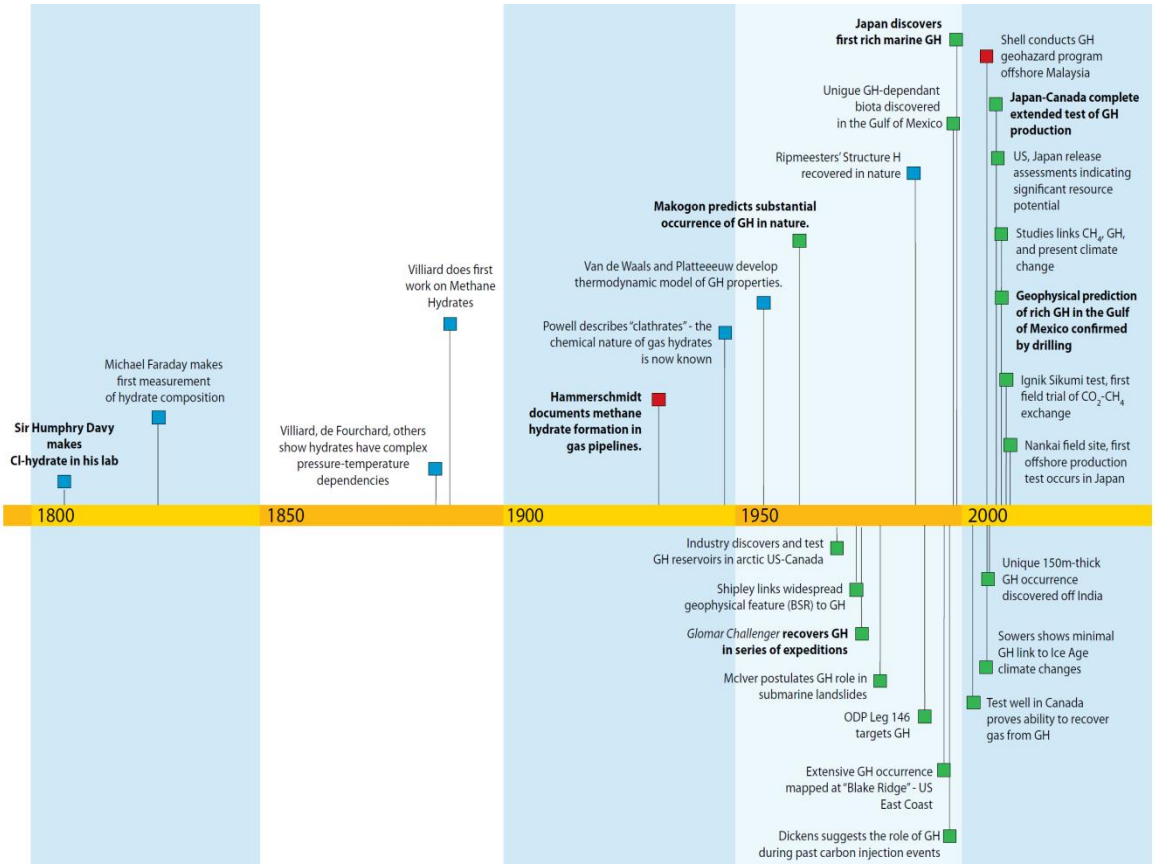

Figure 2.2: Timeline of hydrate studies (Beaudoin et al., 2014)

2.2 CHEMISTRY OF HYDRATES

According to Sloan and Koh (2007), gas hydrates found commonly in nature usually consist of either cubic structure (sI and sII) or hexagonal structure (sH). Field studies suggest Structure I hydrate occurs most often, Structure II is much less common, and Structure H is extremely rare.

Structure I can contain guest molecules of methane, ethane, carbon dioxide and hydrogen sulfide with a diameter between 4.2 to 6 Å. Smaller molecules ($d < 4.2$ Å) such as hydrogen or nitrogen form Structure II. Larger single guest molecules with diameter between 6 to 7 Å such as propane or iso-butane also form Structure II. Molecules with guests such as iso-pentane or neohexane with diameter between 7 to 9 Å along with other smaller molecules such as methane form Structure H.

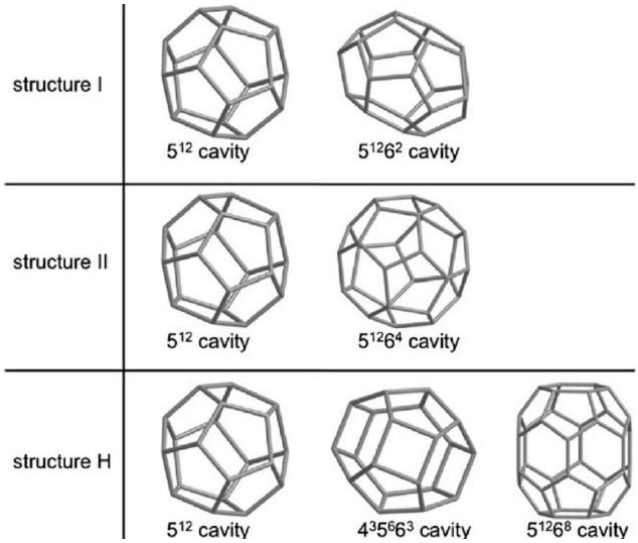

Figure 2.3: Gas hydrate structures (Zheng et al., 2015)

All three hydrate classes (shown in Figure 2.3) have a number of mechanical properties similar to hexagonal ice (Ih) except yield strength and thermal conductivity.

2.2.1 Structure I:

The structure is a primitive cubic lattice with (12-side) pentagonal dodecahedron and (14-side) tetrakaidecahedron cavities represented by 5^{12} and $5^{12}6^2$ respectively. It has vertex-linking of the 5^{12} cavities in three-dimensions and $5^{12}6^2$ cavity is formed between the two 5^{12} cavities. A unit cell is made of $6(5^{12}6^2).2(5^{12}).46H_2O$. There are 46 water molecules inside a structure I cell and eight polyhedra totally inside the cube. Each of the six cube faces contains two halves of $5^{12}6^2$ which gives six $5^{12}6^2$ cavities inside the cell. Each of eight vertices contains one-eighth part of 5^{12} along with one in the centre which adds up to two 5^{12} per cell. Methane hydrates form Structure I (Sloan and Koh, 2007).

2.2.2 Structure II:

The structure II has a face-centred cubic lattice with layers stacked in a staggered pattern ABCABC so centers of the 16-hedra form a diamond lattice within a cube with shared hexagonal faces. A unit cell is made of $8(5^{12}6^4).16(5^{12}).136H_2O$. It has face-

sharing of the 5^{12} cavities in three-dimensions and $5^{12}6^4$ cavity is formed between the two 5^{12} cavities.

2.2.3 Structure H:

Unit cell is made of $1(5^{12}6^8).3(5^{12}).2(4^35^66^3).34H_2O$. It is a hexagonal crystal with $4^35^66^3$ and $5^{12}6^8$ cavities along with 5^{12} cavities. Smaller guest molecules like methane exist in smaller cavities whereas larger ones such as neohexane enter the $5^{12}6^8$ cavity. It has face-sharing in two-dimensions so 5^{12} cavity layer connects a layer of $5^{12}6^8$ and $4^35^66^3$ cavities.

2.3 ENERGY POTENTIAL OF HYDRATES

Unconventional hydrocarbon resources generally require methods such as stimulation to produce them. The different unconventional types such as oil shales, coal bed methane, oil sands and methane hydrates all require specialized extraction techniques with their unique challenges.

Natural gas as an important clean energy resource is becoming increasingly more important. According to the predictions of global gas requirements in the coming years, a number of unconventional hydrocarbon resources will have to be tapped in greater quantities to fulfill the required demand (Beaudoin et al., 2014).

In light of data obtained in recent years, estimates of global in-place hydrate resources have been made in range of 3,000 to 30,000 trillion m^3 (Boswell and Collett, 2006). While a lot of work has been done in quantifying the in-place resources, it is equally important to estimate the volumes of recoverable hydrates. The recent testing results indicate there are massive, wide-spread hydrate resources that can be recovered throughout the world.

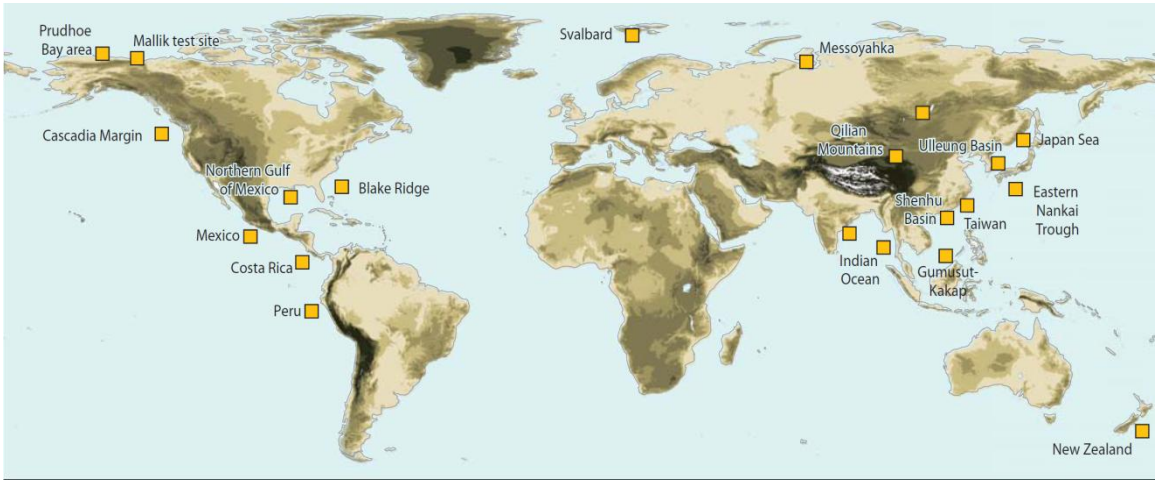

Figure 2.4: Major gas hydrate study areas (Beaudoin et al., 2014)

As seen in Figure 2.4, gas hydrates are observed to be widely distributed throughout the globe in permafrost as well as marine sediments. A number of hydrate deposits are suitably located near countries that do not have substantial reserves of conventional oil and gas. This makes extraction of hydrates an extremely attractive option for countries such as China, India and Japan with access to them.

2.4 GAS HYDRATE PYRAMID

The hydrate resource pyramid was proposed by Boswell and Collett (2006). It is similar to other resource pyramids with the most easily accessible but smallest resource at the peak and progressively larger but more difficult to extract resources below it. The pyramid in Figure 2.5 displays that only partial quantities of the resource can be produced commercially according to ease of extraction.

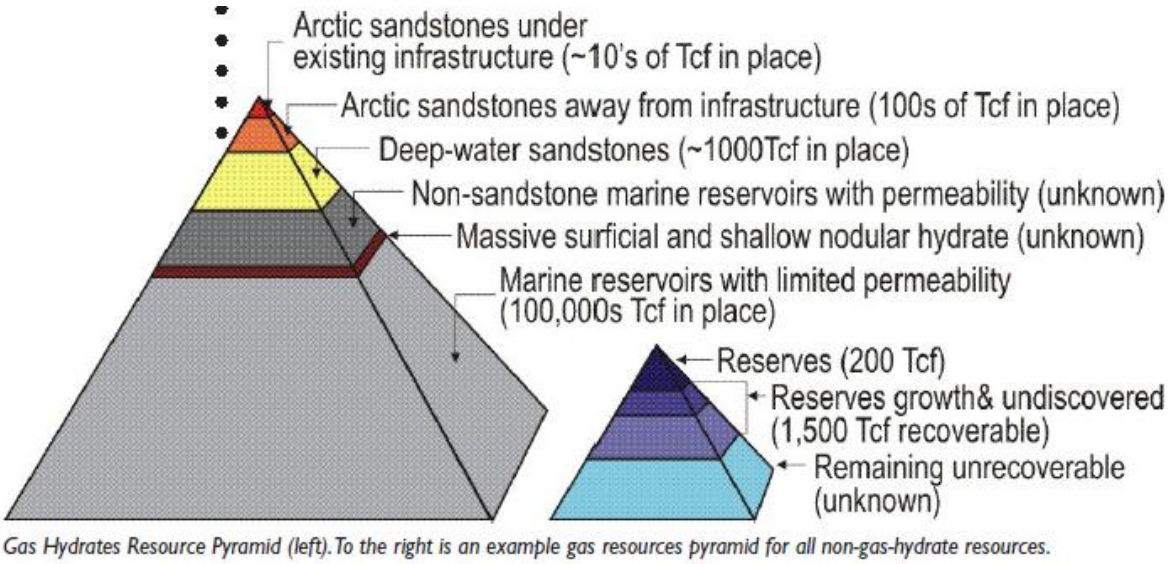

Figure 2.5: Gas hydrate resource pyramid (Boswell and Collett, 2006)

2.4.1 Arctic sand reservoirs:

The top of the pyramid consists of hydrates in arctic permafrost. They are relatively easier to produce than their marine counterparts and in places with accessible infrastructure such as Alaskan North Slope gas production can supply power needs (Hancock, 2004). Short-term production from the Mallik well from Mackenzie Delta in Canada (2002) and Mount Elbert in Alaska (2007) was confirmed by pressure drawdown (Dallimore et al., 2012). Production via CO_2-CH_4 exchange was also tested by ConocoPhilips at Alaska North Slope in the 'Ignik Sikumi' field trial in 2011-2012 (Boswell et al., 2014).

2.4.2 Marine sand reservoirs:

The next category in hydrate resource potential are the high permeability sands in marine sediments. These resources, with sufficient saturation and geology, can prove to contain large quantities of extractable hydrates. As seen in Figure 2.4, studies have shown existence of such sediments in the Gulf of Mexico (Brooks et al., 1984), Vancouver margin (Riedel et al., 2006), Indian Ocean (Collett et al., 2008) and the Malaysian Margin (Hadley et. al., 2008). Marine sands containing high saturations of hydrates were

drilled by a test well in the Nankai Trough in 1999 and sampled in 2004 (Ruppel, 2011). A major milestone was achieved in gas hydrate production technology in 2013 by successful demonstration of gas production from deep water gas hydrates in the turbidite sands located at a depth of 300 meters below sea floor in the Nankai Trough. The gas production was achieved via depressurization using a special electrical submersible pump separating gas and water in separate production strings (Yamamoto, 2015; Boswell et al., 2014). Drilling expeditions undertaken during the DOE-Chevron Joint Industry Program (JIP) have provided evidence of hydrate-rich sands in a number of places in the Gulf of Mexico (Hutchinson et al., 2005; Collett et al., 2012; Boswell et al., 2012; Shelander et al., 2012) which is the focus of this thesis.

2.4.3 Non-sand / low permeability marine sediments:

This section in the resource pyramid is the largest but most technologically challenging. It consists of less-permeable and smaller grained sediments such as silts or clays. At times, hydrates are formed in fractures present within such sediments in places such as Indian or Korean margins (Lee and Collett, 2009). Within the matrix, the hydrate saturations and permeability may be low but due to the massive volumes available, they may prove a viable energy resource in the future with improved technology such as stimulation.

2.5 GAS HYDRATES IN MARINE ENVIRONMENTS

Hydrates in marine sediments are important for a number of reasons in addition to potential future energy resources. They can prove to be potential geohazards in case of slope destabilization and methane being vented to the atmosphere. It has been suggested that dissolution of marine hydrate deposits in the past has been responsible for global climate change (Tréhu et al., 2006). Hydrate studies have also been useful in characterization of the deep biosphere and anaerobic microbial activity.

Hydrate stability is a function of temperature, pressure, the saturation and composition of gas and pore-water. Other factors also important for hydrate growth are sediment grain shape, size and composition.

At atmospheric pressures, methane hydrate is stable at temperatures below -80 °C and hence during conventional coring it was observed that no hydrate could be recovered as a result of depressurization and temperature increase. Pressurized coring mechanisms have since been put to use to get samples of hydrates while preserving them in the in-situ state (Tréhu et al., 2006).

The stability conditions for methane hydrates are fulfilled at all seafloors exceeding 300-800 m (according to local sea temperature). The temperature increases progressively below the sea-floor according to the local thermal gradient and usually several hundred meters below the seafloor, it exceeds the pressure-temperature hydrate stability conditions. While this would allow hydrates to form anywhere, they are also governed by the required methane concentrations in the pore-water which need to be exceeded in order for hydrate precipitation. As a result, most hydrate accumulations occur in continental margins or seas where a sufficient methane supply is present (Tréhu et al., 2006).

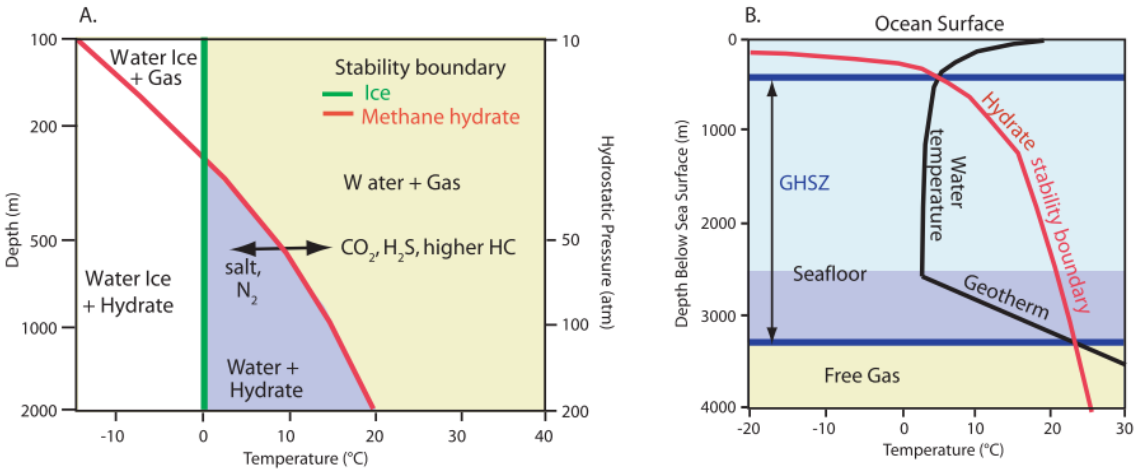

Figure 2.6: Marine gas hydrate stability conditions (Tréhu et al., 2006)

Figure 2.6 describes the methane hydrate stability conditions for marine sediments. The left part is a comparison of the phase boundary for water ice and methane hydrates. With addition of gases such as carbon dioxide, hydrogen sulfide or higher molecular weight hydrocarbons the hydrate boundary shifts to the right while addition of

salt or nitrogen causes the boundary to move to the left. The figure on the right describes the gas hydrate stability zone (GHSZ). The depth and thickness of the GHSZ vary according to the water temperature and the geothermal gradient. The GHSZ thickness below the seafloor is proportional to the water depth considering constant geothermal gradient. It can extend more than a thousand meters below the seafloor (Milkov et al., 2004) but this is still much shallower than depths for exploration of deep-sea conventional hydrocarbons. However, in practicality there exists a methane free zone from seafloor to a certain depth due to anaerobic oxidation of methane by sulfate (Tréhu et al., 2006). In Arctic regions, the GHSZ is about few hundred meters below the top of the permafrost. It can exist at depths of 500 meters below the base of permafrost (Ruppel, 2011).

Methane hydrates are precipitated when methane concentration exceeds solubility in the pore water. Increase in salt concentration inhibits the gas hydrate formation and stability, and the formation of clathrate structure further expels salt and lowers rate of hydrate growth (Liu and Flemings, 2006; Milkov et al., 2004). Based on modeling and experimentation (Uchida et al., 2004), it has been observed that gas hydrate formation is also dependent on the grain characteristics such as shape, size and type of sediments. It is suggested that capillary forces prefer that hydrate is precipitated in coarse-grained sediments rather than fine-grained ones. In finer sediments, hydrates are precipitated more in fractures, veins or higher permeability zones.

2.6 BOTTOM SIMULATING REFLECTION:

Seismic reflection data from deepwater continental margins at times exhibit anomalous, shallow seismic events called 'bottom-simulating reflections' (BSR). They are anomalous in the sense that their orientation does not show relationship with the sedimentary layering but instead they follow the bathymetry of the seafloor, with generally increasing sub-seafloor depth with increasing water depth (Shedd et al., 2012).

The BSR is a result of changing acoustic impedance due to higher-velocity hydrate-bearing material overlying lower-velocity hydrate-free material and it is an indication of hydrate-bearing strata overlying gas bearing strata (Tréhu et al., 2006).

BSR is interpreted to be a very strong indicator for presence of hydrates but absence of a BSR may still allow hydrates to be present. Thus, BSR is a sufficient but not a necessary condition for presence of hydrates. It has been observed that minute gas quantities also affect the seismic velocities. Additionally, the distribution of hydrates in different lithologies also plays a role in the magnitude of observed seismic velocity (Shedd et al., 2012). Availability of downhole logging data is quite useful in such cases for calibration with the seismic data.

2.7 HYDRATE DISTRIBUTION AROUND THE WORLD

Earlier studies predicted hydrates in all marine environments where the temperature-pressure stability conditions were satisfied. Later, when it was recognized that sufficient methane concentrations are a necessary parameter for hydrate precipitation, the estimates were revised by more than an order of magnitude with a more scattered prediction (Beaudoin et al., 2014). Due to the non-uniformity and uncertainty of organic carbon source for methane generation, the exact estimates of hydrate depositions are continuously revised and only estimates can be made of global resource volumes. Nevertheless, it has been observed in a number of cases that marine hydrates tend to be found in continental margins instead of centre of oceanic basins.

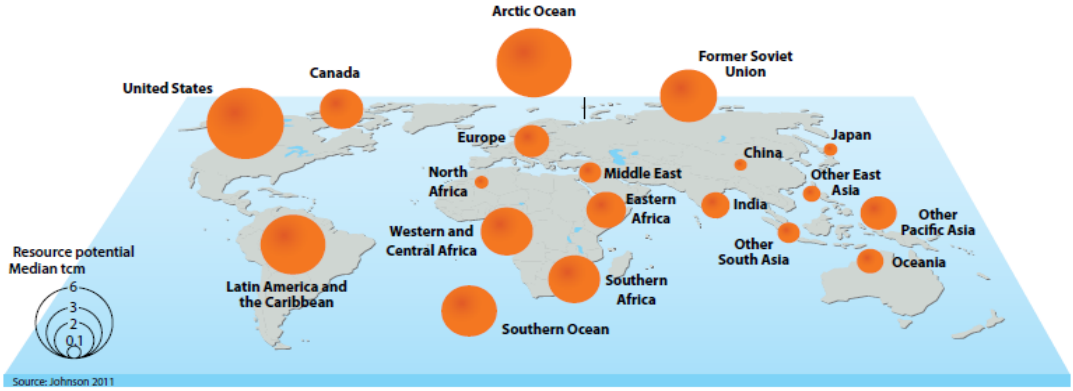

Figure 2.7: Hydrate resource distribution map (Johnson, 2011)

The global hydrate estimates by Johnson (2011) provide a rough order of magnitude of in-place methane hydrate reserves throughout the world. It is seen that there are recoverable reserves distributed throughout the world with cumulative sand reservoir estimates exceeding 1.27 trillion m^3 of gas.

2.8 HYDRATES IN THE NORTHERN GULF OF MEXICO

The Gulf of Mexico is a passive margin petroleum province affected by salt tectonics and has been under special focus in the recent years for hydrate exploration. The northern Gulf of Mexico is a petroleum basin that has been producing oil and gas since 1955 and is one of the most widely drilled continental margins due to its excellent petroleum system (Nehring, 1991).

According to Hutchinson et al., (2008) in the Gulf of Mexico, seafloor spreading occurred in middle of the Mesozoic era. In the middle Cenozoic era, the salt deposited during the Jurassic period was mobilized and affected the surface morphology and stratigraphy of the mini-basins and structural highs. Differential loading of the shelf occurred in the Pliocene-Pleistocene leading to remobilization due to sea level changes. When sea levels were low, the sediments flowed into shelf-edge deltas forming slope basins and fans (Suter and Berryhill, 1985). The viscous salt flows led to creation of basins and highs. Sands were further deposited to deeper locations due to mass-wasting. During higher sea levels such as the present Holocene epoch, sediments were left in a landward position due to retreating deltas leaving the slopes and rises without sediments. The hydrocarbons are observed to seep to the seafloor along conduits near edge of sub-sea salt deposits with both thermogenic and biogenic sources (Roberts, 1995).

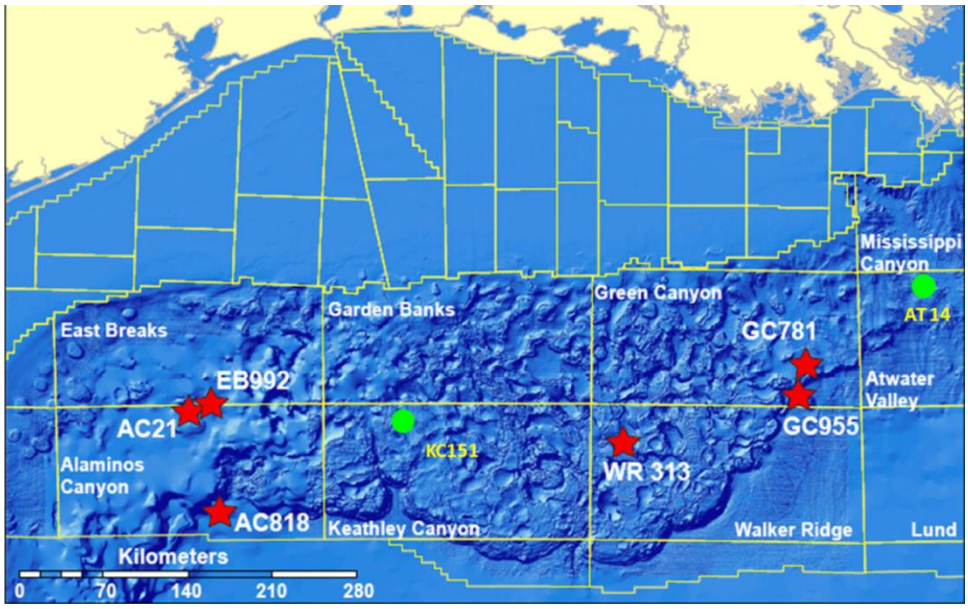

Figure 2.8: Gas hydrate sites in Gulf of Mexico (Birchwood and Noeth, 2012). AC = Alaminos Canyon; AT = Atwater Valley; EB = East Breaks; GC = Green Canyon; KC = Keathley Canyon; WR = Walker Ridge.

The Figure 2.8 shows the different drilling sites investigated in the Northern Gulf of Mexico. Circles denote sites investigated during first phase of JIP in 2005 and stars denote sites investigated in 2009 during second phase.

A study undertaken by Frye in 2008 found massive quantities of gas hydrate as a result of seismic and well data analysis. It is estimated that there is more than 991 trillion m^3 of gas in the basin. Due to a number of subsea hydrate seepages observed, hydrate depositions were investigated to prevent hazards while drilling. Frye (2008) estimated gas in place resources of hydrates as high as 607 trillion ft^3. A number of sites in different parts of Gulf of Mexico were drilled in 2005 and 2009 according to the Chevron-DOE JIP based on pre-drilling data and six of them in 2009 discovered hydrates in sand reservoirs (Shelander et al., 2010). With hydrate presence as deep as 800 meters below sea-floor, Gulf of Mexico promises to be a potential source for production of hydrates in the coming years and is therefore studied for this project.

Chapter 3: Prediction of pore size distribution

As pore size distribution data is not available for Walker Ridge 313 Block, synthetic nuclear magnetic resonance (NMR) relaxation time distribution was generated by comparison with NMR data available at Keathley Canyon. Information about Keathley Canyon (KC), Walker Ridge (WR) and the procedure involved in calculations is described in detail in this Chapter.

3.1 KEATHLEY CANYON 151 GAS HYDRATE SITE: BACKGROUND

The drilling in KC-151 as a part of JIP Leg-I in 2005 confirmed the pre-drill interpretations of hydrate occurrences from the seismic data. Log data showed that hydrate was prevalent in high-angle fractures in the clay-rich sediments and within the pores in coarser-grained sediments. The drilling results indicated that the low-saturation hydrates in the fine-grained sediments were not a major drilling hazard and can be controlled by controlling the well-bore pressure and temperature (Hutchinson et al., 2008).

Drillsite KC 151-2 (26.8229 °N, 92.9864 °W) is located along the south-eastern edge of the intraslope Casey Basin about 131 km west of Walker Ridge 313 (Figure 3.1). KC 151-2 was drilled and logged with logging-while-drilling (LWD) tools. KC-151-3 located ~10 m from KC-151-2 was cored and wireline logged (Cook et al., 2008).

Figure 3.1: Location of KC151 and WR313 in Gulf of Mexico

The Casey Basin is roughly 12 km wide and is elongated in northwest-southeast direction. The basin has an opening towards the south with the deepest point being around 1470 m (Boswell et al., 2012). The thickness of the GHSZ around the KC-151-2 well is estimated to increase from 250 m at basin edges to more than 400 m towards the centre of the basin according to the BSR data.

3.2 KEATHLEY CANYON-151: DRILLING AND LOGGING RESULTS

KC-151-2 was drilled to a total depth of 459 m below sea floor (mbsf) and logs including caliper, gamma ray, resistivity-at-bit, neutron porosity, bulk density, and nuclear magnetic resonance were recorded. Gamma ray, ultrasonic caliper, ring resistivity, and bulk density are shown in Figure 3.2.

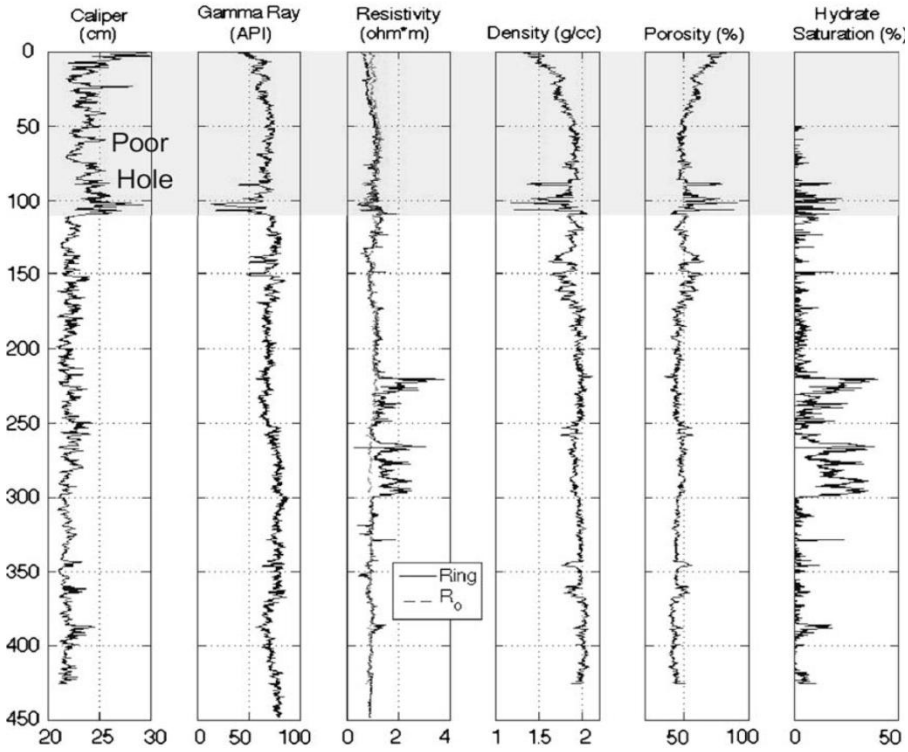

Figure 3.2: KC-151-2 logs (Cook et al., 2008)

In Figure 3.2, the shaded region above ~115 m depth indicates a zone of poor log quality due to poor borehole conditions. The resistivity curves shown include the ring

resistivity from the resistivity-at-bit tool as well as a calculated R_o curve, which indicates the resistivity of the formation if it were 100% water-saturated. Differences between the ring resistivity and R_o are interpreted to be due to the presence of hydrate.

The caliper shows that the hole diameter has enlarged by about 2.5 to 7.5 cm from the standard 21.5 cm in the interval 0 to 115 mbsf, resulting in lower data quality (Cook et al., 2008). The most enlarged borehole was observed in the depths of 100 to 115 mbsf correlating to a sandy clay unit. The log quality is good from depth of 115 to 459 mbsf with relatively smooth and regular hole geometry allowing high quality log readings. Gamma ray (GR), porosity, and nuclear magnetic resonance (NMR) logs are discussed in detail below.

3.2.1 GR log:

Figure 3.3 shows the GR log recorded.

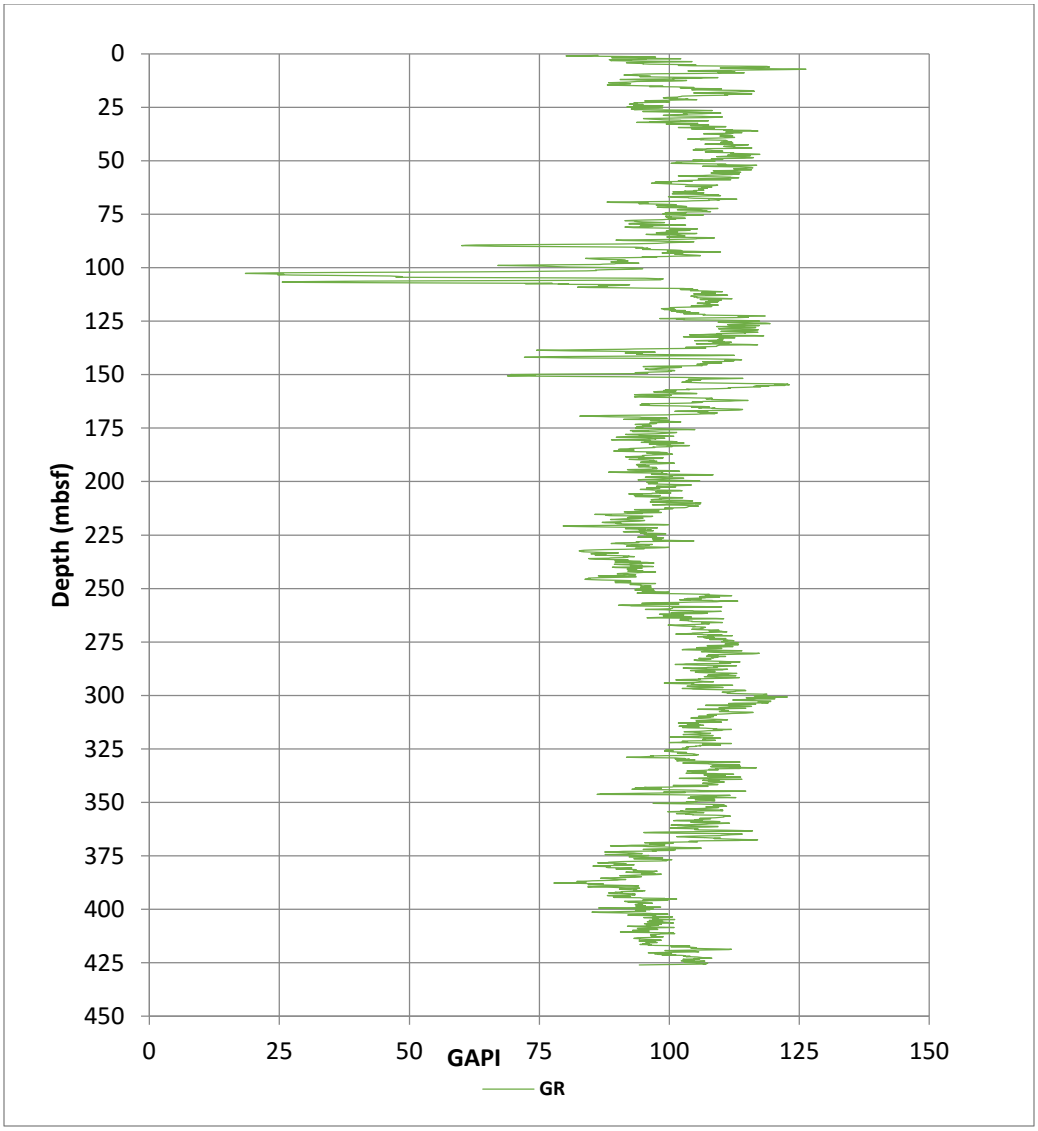

Figure 3.3: GR log in KC-151-2

Hutchinson et al., (2008) conducted an analysis to link the seismic stratigraphy with well data for KC-151-2. Gamma ray log data correlated with interpreted seismic stratigraphy showed lithographic changes at various depths. It can be seen that gamma ray values dip by 40 GAPI in 100-115 mbsf indicating a sandy layer. Similarly, a spike in gamma ray around 140 mbsf translates into sandy lithology. A disconformity correlated with a gamma ray spike was seen at 150 mbsf which may be a coarser boundary. The

greater depths are devoid of large gamma ray spikes indicating absence of sand layers and presence of clay sediments or fine-grained turbidites.

3.2.2 Porosity:

The porosity (Figure 3.4) has been calculated from the density log since porosity is a function of the density of the formation and of the pore-filled fluid (assumed to be water). The formula utilized is:

$$\phi = \frac{(\rho s - \rho b)}{(\rho s - \rho f)} \ , \tag{1}$$

where ρ_b is in-situ formation density (from density log),

ρ_s is grain density (2.65 gm/cm^3 in sands, 2.70 gm/cm^3 in clays),

ρ_f is pore-water density (1.03 gm/cm^3).

The values are normal for shallow marine clays and the trend that is shown is a likely result of slow compaction with burial. Corrections were made for high saturation hydrates and poor hole conditions (Daigle et al., 2015).

Density log is preferred for porosity calculations rather than neutron porosity logs because the neutron porosity log measures hydrogen index and in unconsolidated clays it responds to the hydrogen in clays and clay bound water in addition to in situ fluids. This gives an overestimated value of porosity. The neutron porosity logs however are still useful in the gas zones to indicate gas with lower hydrogen index than water (Cook et al., 2008).

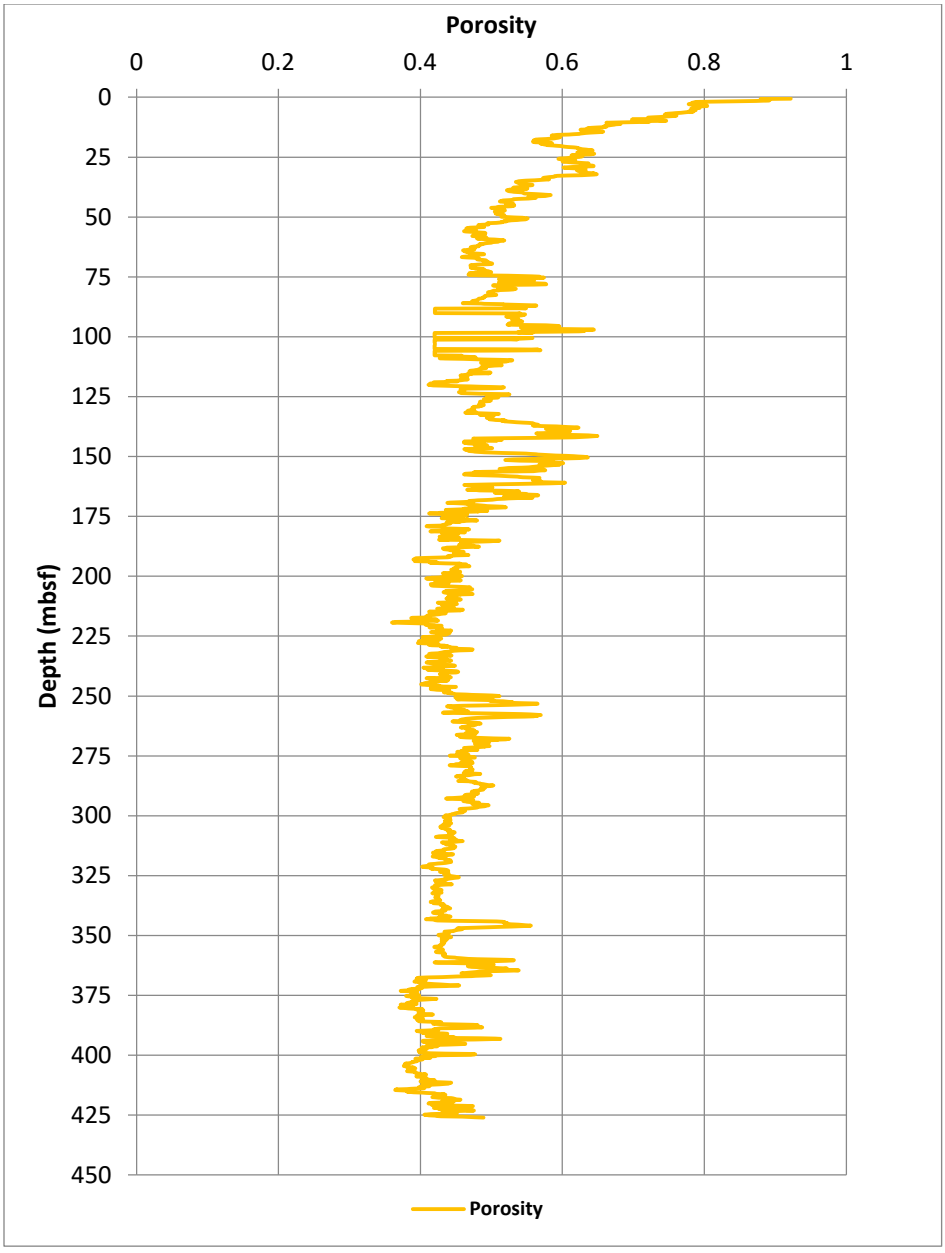

Figure 3.4: Porosity in KC-151-2

3.2.3 NMR log:

The NMR measurements were conducted by Schlumberger's ProVISION^{TM} tool, which used a set of antennas to focus a cylindrically shaped magnetic field on the formation. The vertical resolution of the tool was between 1 and 1.2 m with a depth of

investigation about 7 cm in a 21.5 cm borehole (Daigle and Dugan, 2009). From the measured NMR log, the transverse relaxation time (T_2) was calculated. The NMR log measures different amplitudes for the various T_2 values according to the formation and fluid at any particular depth.

For an easier characterization of the NMR data, the relaxation time distribution was converted into Log Mean of T_2 (MLT2) and Standard Deviation (SD) according to the following formulae:

$$Mean : \overline{LogT\ 2} = \frac{\sum_{i}^{n} (ai \times LogT\ 2i)}{\sum_{i}^{n} (ai)}, \tag{2}$$

$$SD = \sqrt{\frac{\sum_{i}^{n} (LogT2 - \overline{LogT2})^2}{n}}, \tag{3}$$

where n = 30 (number of data sample points along the distribution) and ai = amplitude.

MLT2 and SD are plotted versus depth in Figure 3.5.

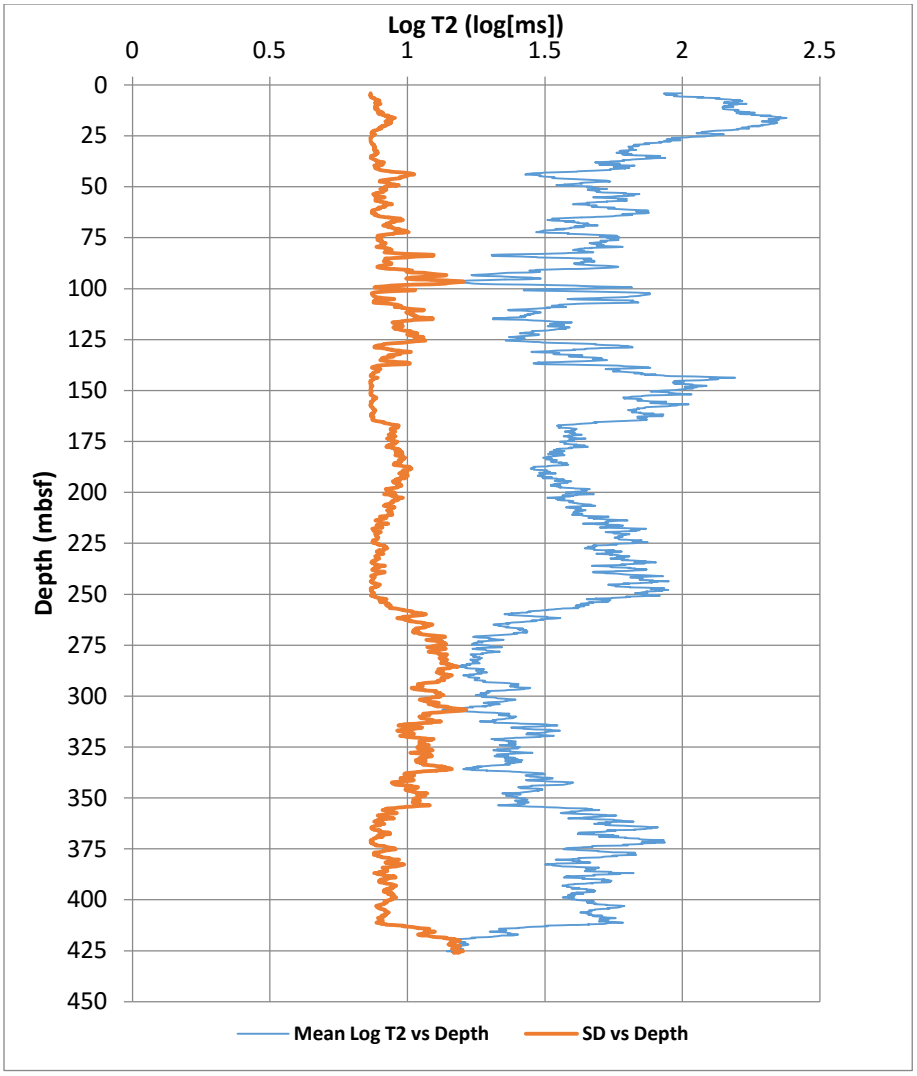

Figure 3.5: MLT2 and SD in KC-151-2

3.2.4 Gas hydrates at KC-151:

Hydrate saturation was computed at this site by Archie's law (1942) for known values of resistivity and Archie constants.

$$S_h = 1 - \left(\frac{aR_w}{\Phi^m R_t}\right)^{1/n} \quad , \tag{4}$$

where R_t is measured resistivity,

R_w is calculated resistivity,

n is cementation exponent for marine sands (n = 2.4) (Cook et al., 2008),

m is saturation exponent for marine sands (m = 1.22) (Cook et al., 2008),

a is tortuosity factor for marine sands (a = 2.19) (Cook et al., 2008).

During drilling, gas hydrate samples were not recovered but evidence from electrical resistivity anomaly and cold spots in the cores suggest presence of hydrates in depth range of 220 - 300 mbsf. This depth interval contains fine-grained mud and clays according to logging and seismic data.

According to Cook et al. (2008), the hydrates occur primarily in two modes:

i) Filling open fractures

ii) Filling permeable beds

The hydrates mostly reside in fractures due to the low permeability of the clays. Some natural gas may move from fracture conduits into permeable bedding layers, forming hydrate in those layers. Such hydrate-filled beds were interpreted at 109 mbsf, 231-235 mbsf and 306 mbsf near hydrate filled fractures (Cook et al., 2008). A slight resistivity anomaly around depth of 392 mbsf may be the BSR (Lee and Collett, 2008) correlatable with a weak reflection.

The site KC-151 contains more than 50 m of hydrate bearing sediments with saturation greater than 20% which is significant compared to other marine hydrate accumulations (Cook et al., 2008).

3.3 WALKER RIDGE 313 GAS HYDRATE SITE: BACKGROUND

Walker Ridge is an area of hydrocarbon exploration situated in the deepwater northern Gulf of Mexico. The Gulf of Mexico Gas Hydrate Joint Industry Project conducted Leg II in April-May 2009 in the northern Gulf of Mexico. Seven wells were drilled in total in Leg II, out of which two were in Walker Ridge Block 313 (Frye et al., 2012).

In 2001, a single industry well, WR-313-1, was drilled by Ocean Energy to a total measured depth of 5096 m below sea level in the area targeting deeper hydrocarbon

targets and was formally termed as OCS-G-18683 #001. It was later abandoned and the logs through the hydrate stability zone were of poor quality.

First indications of gas hydrates in the area were observed by McConnell and Kendall (2002) by a recognition of the base of gas hydrate stability (BGHS) from seismic data. They also showed that the depth of the BGHS coincided with the modeled phase stability curve. Other work (McConnell and Zhang, 2005) includes recognition of phase reversal of seismic wavelets as a series of anomalous seismic responses at BGHS indicating presence of a BSR. The configuration indicated a buoyant separation of free gas and water inside the permeable and porous units where the accumulations of hydrates up-dip caused a barrier for further gas migration (Boswell et al., 2012).

According to Hutchinson et al., (2005), the Walker Ridge site fulfilled all the necessary conditions of an active petroleum system. There are faults existing both extensional above salt and compressional at center of the basin. Fluid expulsion is present from mounds on the sea floor and sand or (sand-silt) units have expected lithologies for a reservoir. The clay units serve as impermeable seals to the system. Walker Ridge has a cyclical stratigraphy with alternating coarse and fine-grained sediments which can allow methane-charged fluids to migrate along the stratigraphy in addition to structural faults or fractures. To target the gas hydrate prospects to west of WR-313-1, wells WR-313-G and WR-313-H were planned and drilled as proposed by Hutchinson et al. (2005).

3.4 WALKER RIDGE GEOLOGY

The Terrebonne basin is located in the middle slope of the tabular salt and mini-basin province of the northern Gulf of Mexico. It is a salt-bounded and salt-floored secondary sedimentary basin with location in the north-western part of Walker Ridge planning area. The basin as seen in Figure 3.6 has dimensions of approximately 25 miles in north-south direction, with about 15 miles extent in east-west direction at its southern-most point which is divided into two lobes. The gravity-driven flows from the north deliver clastic sediments to the basin. The factors like supply of sediments, sea level fluctuation, subsidence and basin morphology played a role in determining the

sedimentation rate (Frye et al., 2012). This gravity-driven flow was focused in the axial portions of the sub-basins and allowed reduced-to-reverse gradients which reduced the channelized facies and caused deposition of 'ponded' turbiditic sands (Boswell et al., 2012).

It is inferred from paleontological data that the south-western lobe has been an active depocenter for the past 15 million years. The hydrate targets in the wells are of lower Pleistocene and younger age. According to stratigraphic data, Miocene and Pliocene age sections in the area are more sand-rich than the Pleistocene and Holocene sections, which are more mud-dominated (Frye et al., 2012). The system changed from a sand-dominated to a mud-dominated one when the deepwater sand deposition in the area ended. A rapid vertical salt movement was responsible for separation of both lobes near the southern margin and is responsible for most of the formation of the hydrate sand targets. There are several post-tectonic depositional mud-dominated sequences with relatively uniform gross interval thickness in later periods.

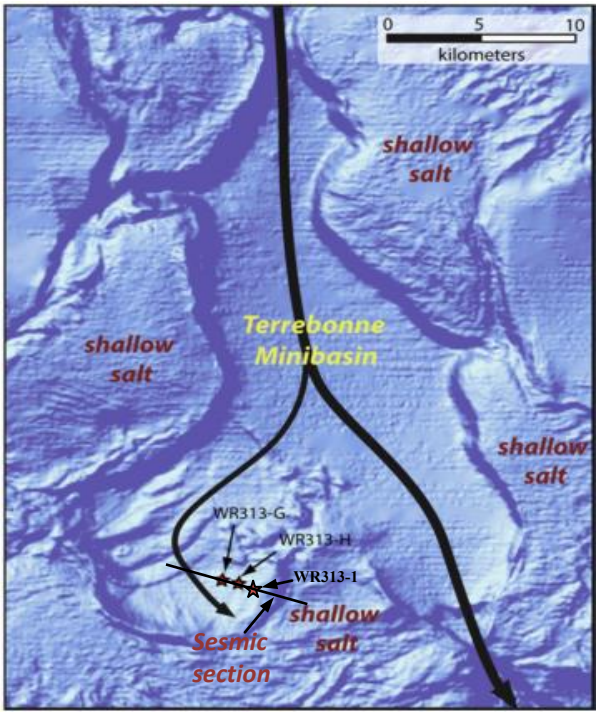

Figure 3.6: Location of WR wells in Terrebonne basin (Boswell et al., 2012)

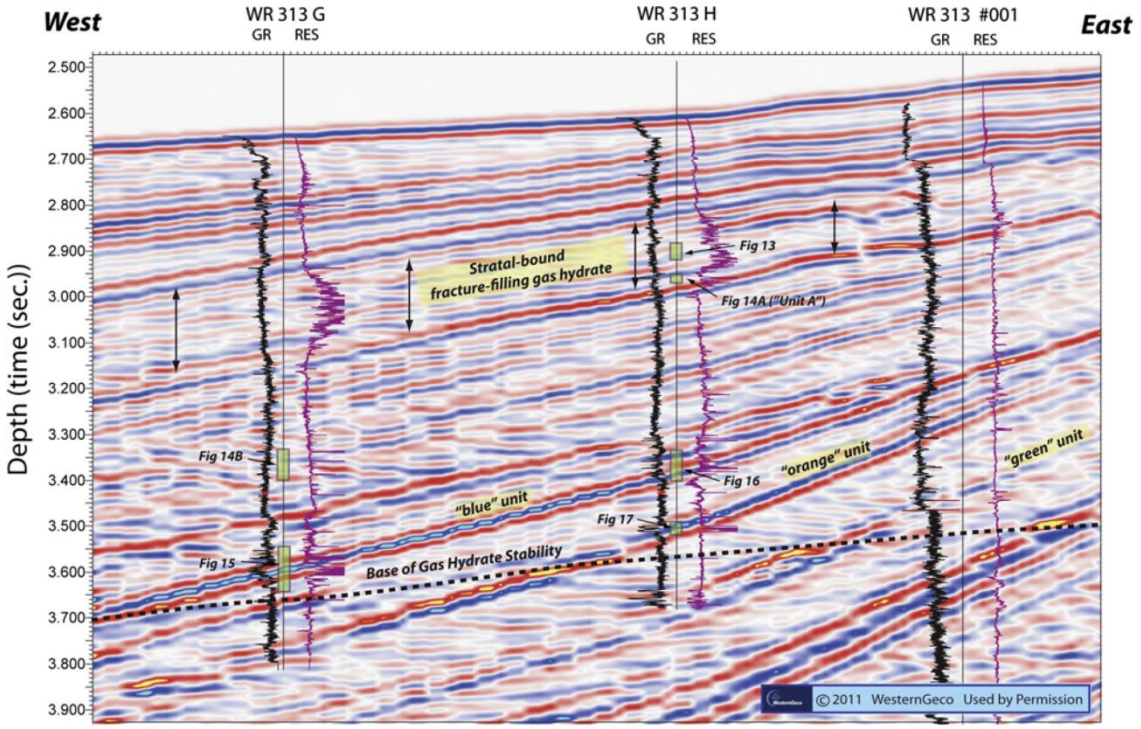

Figure 3.7: Seismic section of WR wells (Boswell et al., 2012)

Figure 3.7 shows a seismic section of the three wells at Walker Ridge slightly inclined in the northwest-southeast direction. The stratigraphy is observed to be dipping in the northwest direction by about 7 to 12°.

Table 3.1 shows the depths of sands encountered and the hydrate zone net thickness for all the three wells at Walker Ridge (Frye et al., 2012). Since WR-313-G is the most down-dip drilled well, it encountered gas hydrate only in the blue sand and hence has hydrate zone in the other sands marked either missing or not recorded.

Horizon	**Depth/Thickness (mbsf)**	**WR-313-G**	**WR-313-H**	**WR-313-1**
Blue Sand	Top	774	650	547
	Bottom	878	702	582
	GH net thickness	11	3	2

Horizon	Depth/Thickness (mbsf)	WR-313-G	WR-313-H	WR-313-1
Orange Sand	Top	Missing	806	638
	Bottom	Missing	819	645
	GH net thickness	-	8	2
Green Sand	Top	NR	952	777
	Bottom	NR	990	805
	GH net thickness	-	-	5
Pink Sand	Top	NR	NR	975
	Bottom	NR	NR	1045
	GH net thickness	-	-	-
BGHS		~949	~900	~850

Table 3.1: Stratigraphic details of wells at WR-313. NR = not recorded.

3.5 WALKER RIDGE 313: DRILLING AND LOGGING RESULTS

3.5.1 Well WR-313-G:

WR-313G was the first well drilled at the WR-313 site during the Leg II campaign in 2009 with co-ordinates: 26° 39' 47.4841" N, 91° 41' 01.9404" W to a depth of 1092 mbsf (Collett et al., 2012). It is the most downdip of the three wells and primarily aimed to test the Blue sand which is just above the BGHS. The Blue interval has gross thickness of about 100 m with ~3 m clean periodic sands with high resistivity and fast acoustic velocity indicating the presence of hydrate. The net gas hydrate in the interval is estimated to be about 11 m with about 40% hydrate saturation in most laminations as seen in Figure 3.8 (Boswell et al., 2012).

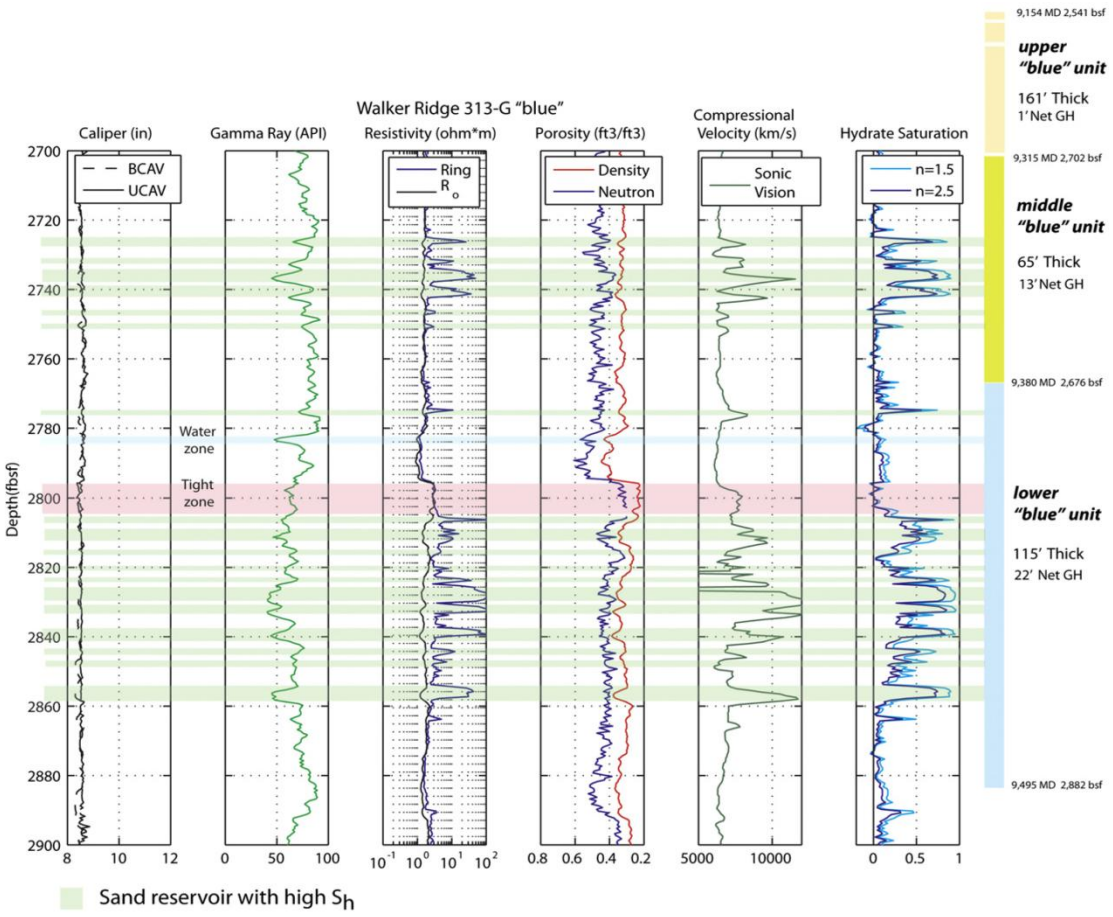

Figure 3.8: Saturation in the Blue sand at WR-313-G (Boswell et al., 2012)

The secondary target of the well was the Orange sand which LWD indicated was a clay-rich interval below the BGHS. The well also targeted other intervals such as a shallow (237 to 402 mbsf) thick, fine-grained unit with hydrate-filled fractures inside fine sediments.

3.5.2 Well WR-313-H:

This well was drilled about 1 km updip to the east of WR-313-G with coordinates: 26° 39' 44.8482" N, 91° 40' 33.7467" W to a depth of 996 mbsf (Collett et al., 2012). The primary objective of this well was to test the Orange interval which lies above the BGHS at this location. The sand was penetrated at a depth of 806 mbsf as two separate hydrate-saturated bodies. The sand showed a low GR signature along with high resistivity and

high acoustic velocity. The gross thickness of the sand was calculated to be 13 m (Upper sand: 4 m and Lower sand: 7 m). Saturations for both upper and lower units were calculated to be 75-90% and 40-70% as seen in Figure 3.9 (Boswell et al., 2012).

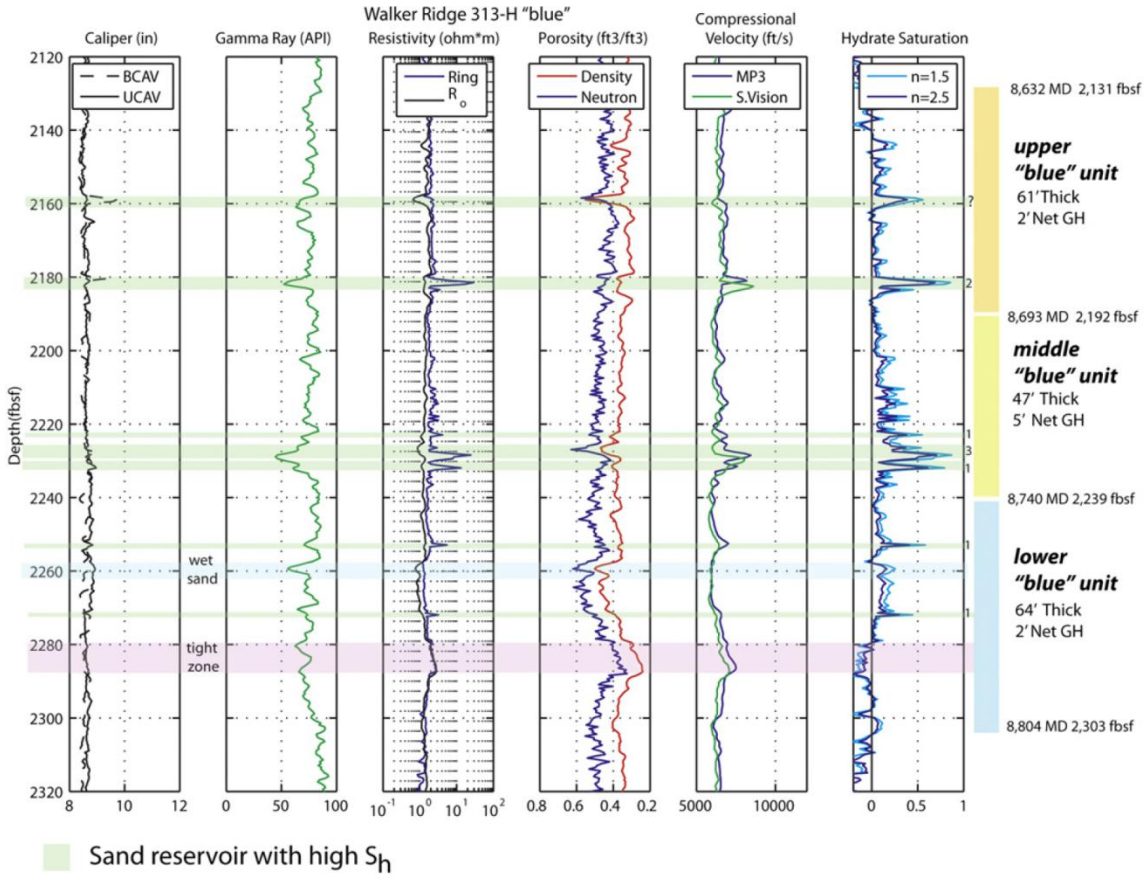

Figure 3.9a: Saturation in the Blue sand at WR-313-H (Boswell et al., 2012)

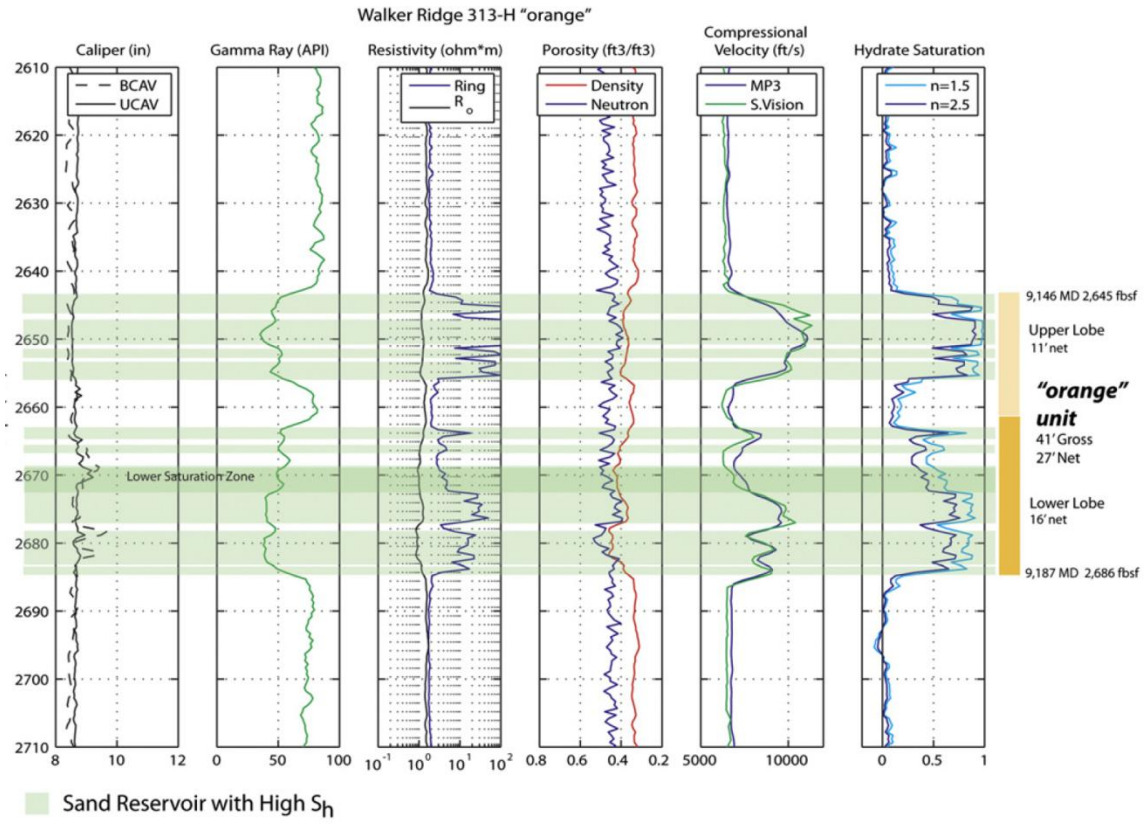

Figure 3.9b: Saturation in the Orange sand at WR-313-H (Boswell et al., 2012)

The well also tested the Blue sand about 200 m updip of its position in WR-313-G well. The sand was encountered at 650 mbsf with a thickness of 52 m. Due to its clayey nature, the net thickness of the sand was only about 3 m. The well also penetrated the Green sand at a depth of 952 mbsf with gross thickness of 38 m. This sand, while non-hydrate bearing, served as a reference for calibration for the other intervals. Another interval that was investigated was the shallow clay-rich interval also seen in the WR-313-H well (Collett et al., 2012).

3.5.3 Well WR-313-001 (OCS-G 18683 #001):

This well was drilled to a depth of 3158 mbsf by Ocean Energy to target reservoirs in the Titan South prospect. Since it did not encounter commercial hydrocarbons, it was abandoned. The GR data was poor but the resistivity data was able to recognize thin sands in shallower depths.

It encountered the mud-dominated Blue sand at 547 m with gross thickness of 36 m. The net thickness of hydrate bearing sands was estimated to be around 2 m. Orange sand was penetrated at a depth of 638 mbsf and had gross thickness of 7 m; the upper unit had 1 m of hydrate and lower had 1.5 m of hydrate deposition. Green sand interval was reached at 777 mbsf. The gross thickness was about 30 m with hydrate thickness ~5 m. The well finally encountered the clay-prone Pink sand at 975 mbsf with gross thickness of 70 m. The Pink sand was not encountered by the other two wells (Boswell et al., 2012).

3.6 HORIZONS AT WR-313:

As shown in Figure 3.10; the Blue, Orange, Green and Pink sand target intervals were the interpreted horizons from seismic data (Frye et al., 2012).

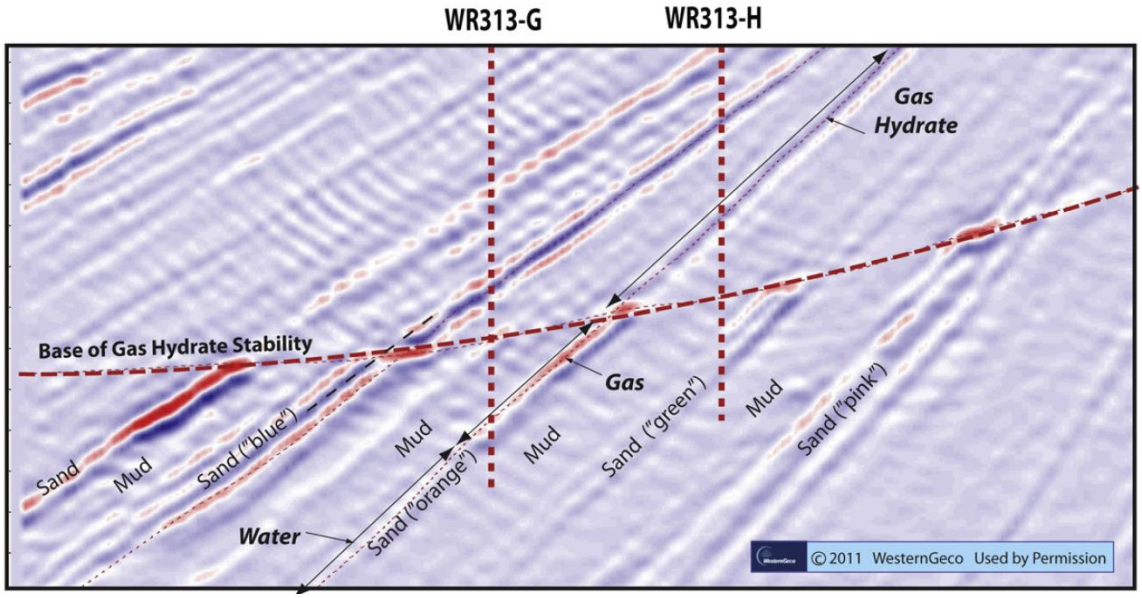

Figure 3.10: Interpreted seismic section at WR-313 (Boswell et al., 2012)

Out of the various stratigraphic units in the Terrebonne basin the reservoirs Blue sand and Orange sand are relevant for this work and are therefore discussed in greater detail.

3.6.1 Blue horizon:

As seen in Figure 3.10, the blue horizon wavelet, if observed, reverses its polarity at BGHS and becomes a seismic trough. The lower part of the Blue sand has the highest saturation in the Blue unit and has the coarsest lithology. As the horizon is traced downdip, the gross thickness goes on decreasing from 35 m in WR-313-1 to 11 m in WR-313-G. It is a mud-rich intraslope ponded submarine fan complex, with both sand sheets and leveed channels (Frye et al., 2012).

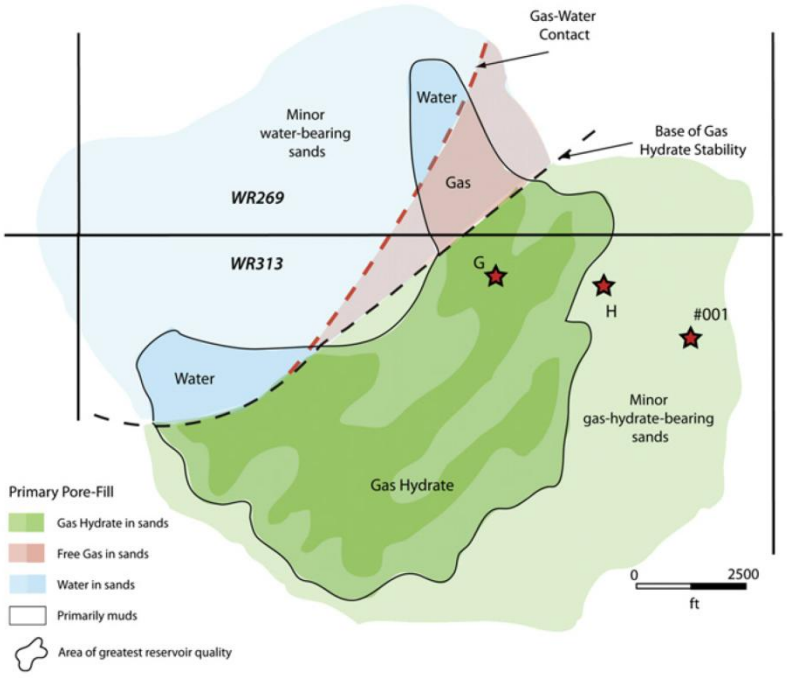

Figure 3.11: Lithological map of Blue sand (Boswell et al., 2012). Colors indicate the fluids in the pore space as interpreted from seismic data. Darker colors correspond to higher certainty in the interpretation.

The Figure 3.11 shows the lithology and pore-fill for the Blue Sand. Areas inside heavy lines indicate best reservoir quality. As it can be seen, the transition from hydrate to gas occurs downdip of the WR-313-G well (along the north-west direction). The LWD data indicated that porosity for the Blue sand at WR-313-H was about 33% and 39% in

shallower depths. The hydrate saturation commonly exceeds 60% and in better developed sands at WR-313-G is expected to be greater than 80 % (Boswell et al., 2012).

3.6.2 Orange horizon:

In Figure 3.10, the nature of the response from an anomalously strong seismic wavelet when traced downdip, reverses polarity at the BGHS to become a seismic trough, which is a strong sign that channel sands are gas saturated below the BGHS and hydrate-saturated above them. However, this wasn't tested during drilling (Boswell et al., 2012).

It is interpreted to have been deposited as low sand concentration turbidity currents in a partially confined basin setting with bounding salts on east and south. Thinning of the gross thickness is seen between WR-313-H and WR-313-1 wells. Lateral variation in the thickness is indicated by the seismic amplitude response. A channel intrudes into the sand along NW-SE and a number of stacked and combined channels are seen in the channel architecture.

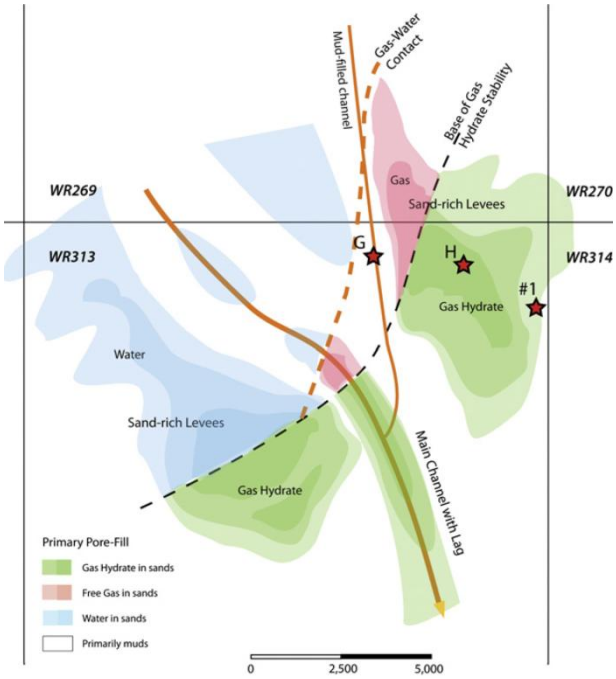

Figure 3.12: Lithological map of Orange sand (Boswell et al., 2012)

The Figure 3.12 shows lithology and pore fill for Orange sand. It shows an axial channel with channel lag as well as smaller mud-filled channels and sand-rich levees. The

well WR-313-G was drilled near a mud-filled channel to avoid free-gas bearing sand while WR-313-H was drilled on northern margin of major channel feature just updip of the BGHS to test the unit where there was a strong positive seismic response (Boswell et al., 2012).

The sand part of the Orange sand updip of the BGHS contains hydrates and calculations show average hydrate saturations to be round 70% with range from 50-90 %.

The porosity in the upper unit was measured to be ~37% with hydrate saturations about 60-90 %. In the lower unit, the porosity was about 40% while the hydrate saturation was calculated to be about 30-60%.

3.7 SYNTHETIC LOG GENERATION

In the absence of NMR logs and pore size distribution data at Walker Ridge, synthetic relaxation time distribution data (NMR) was generated using log data available at Keathley Canyon.

At KC-151-2, it is seen that the GR log is directly proportional to SD but is inversely proportional to the MLT2. When the sediment size (and corresponding pore size) is larger, the GR shows lower values but the larger pore size causes the mean T_2 to increase. At the same time, with better sorting and similarly sized grains the SD value is lowered. The exact opposite phenomena occurs when the GR values goes lower in case of clays causing a lower mean T_2 and higher SD. The porosity is also observed to be having a trend directly proportional to SD and inversely proportional to MLT2.

Figures-3.13, 3.14, 3.15, 3.16 are cross-plots between the different variables. The plots show that SD and MLT2 are functions of GR and porosity.

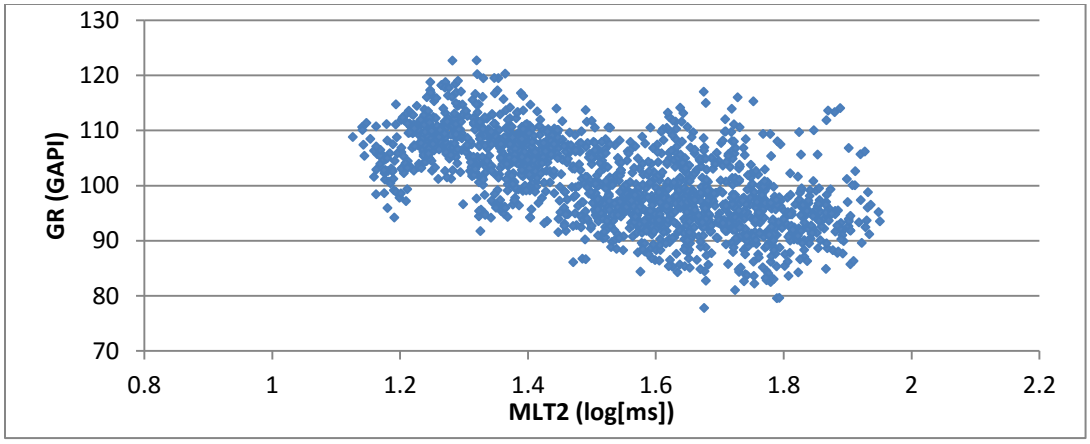

Figure 3.13: Cross-plot of MLT2 and GR shows inverse correlation

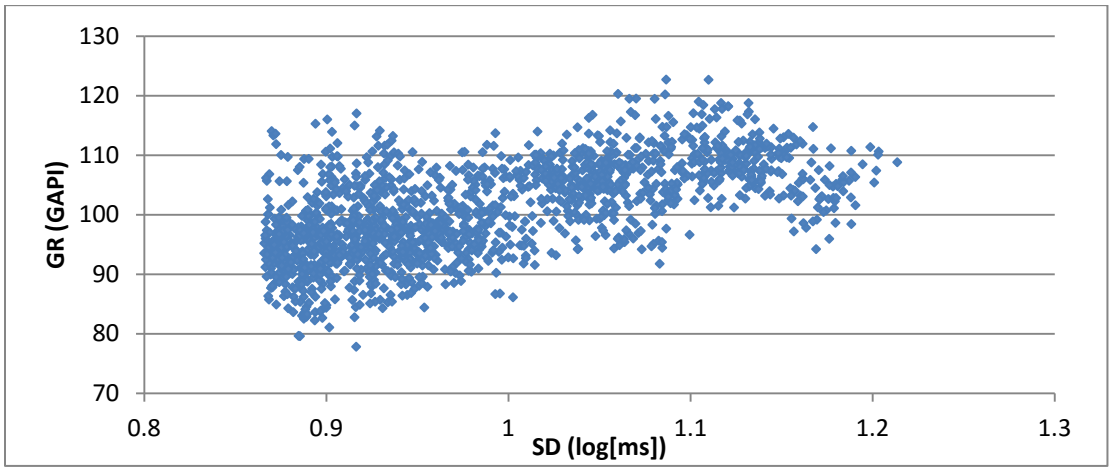

Figure 3.14: Cross-plot of SD and GR shows direct correlation

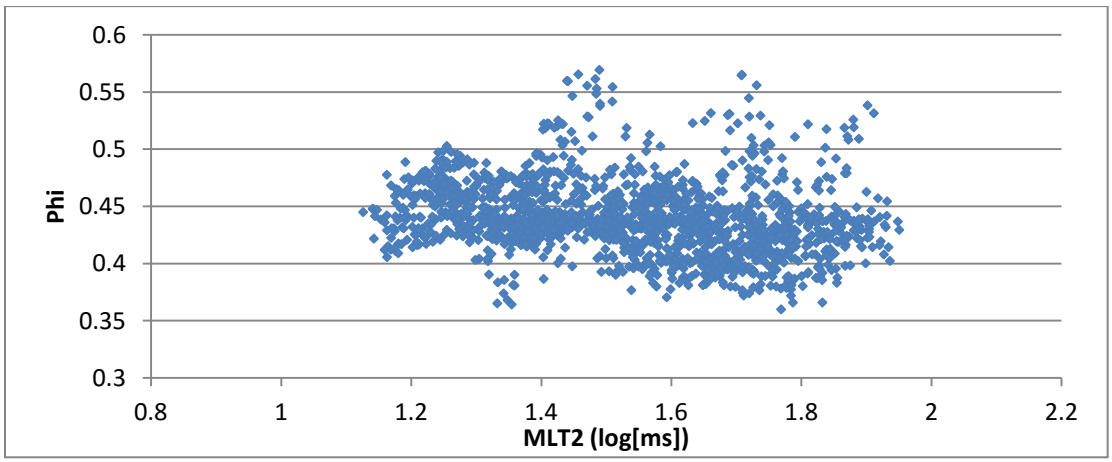

Figure 3.15: Cross-plot of MLT2 and Phi shows weakly inverse correlation

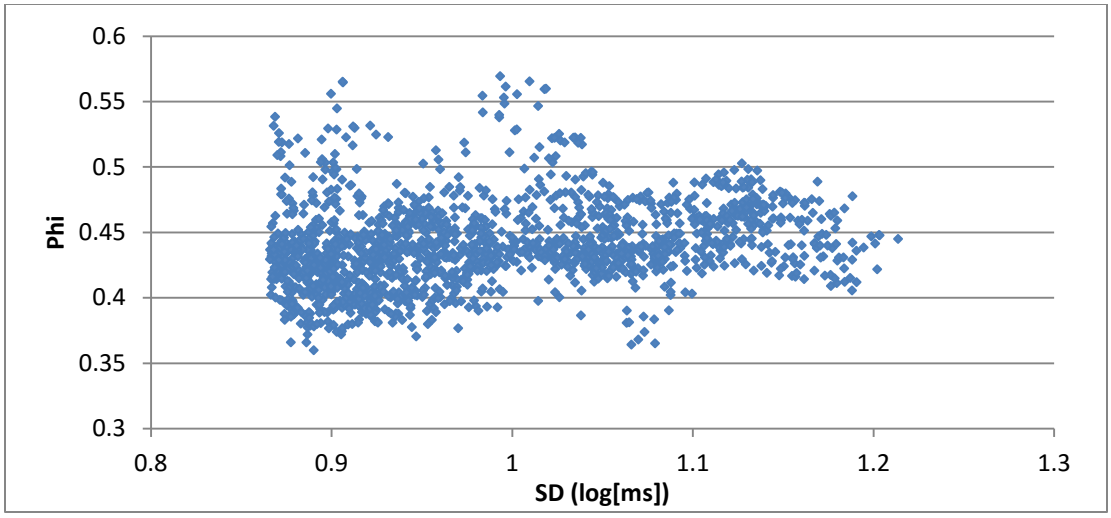

Figure 3.16: Cross-plot of SD and Phi shows weakly direct correlation

The figures indicate a relation between GR and porosity with the MLT2 and SD. Therefore, regression analysis was further utilized for generation of synthetic NMR logs.

3.8 Regression Analysis

The regression analysis was conducted using IBM's SPSS statistics software package. SPSS can be used for data management, descriptive statistical analysis or for inferential and multivariate procedures such as analysis of variance (ANOVA) and regression analysis.

The multivariate non-linear regression analysis involved prediction of MLT2 and SD by constructing correlations using independent variables (GR and porosity data) for all depths of well KC-151-2. During the preliminary study, it was seen that data shallower than 175 mbsf was inconsistent, with excessive data scatter due to bad hole conditions as discussed earlier and therefore the data was excluded during the regression.

The data then contained 1647 samples on which an initial multi-variable regression was conducted for both MLT2 and SD by ordinary least squares method with gamma ray and porosity as the independent variables. It was found that 8 of the data points were unreliable and affected the correlation adversely; hence these outliers were discarded.

After various trials and combinations, it was observed that a correlation of the following form gave best fit:

$$\boldsymbol{MLT2 = a + b \times GR + c \times \Phi + d \times GR^2 + e \times \Phi^2 + f \times \Phi \times GR} \quad , \qquad (5)$$

$$\boldsymbol{SD = a + b \times GR + c \times \Phi + d \times GR^2 + e \times \Phi^2 + f \times \Phi \times GR} \quad , \qquad (6)$$

3.8.1 Regression for MLT2:

It was established from analysis that homoscedasticity was maintained, i.e., there existed homogeneity of variance. Multicollinearity was assessed (tolerance= 1.0) and it was seen that the independent variables were not highly inter-correlated. Normal distribution of data was confirmed from a histogram of residuals as seen from Figure 3.17.

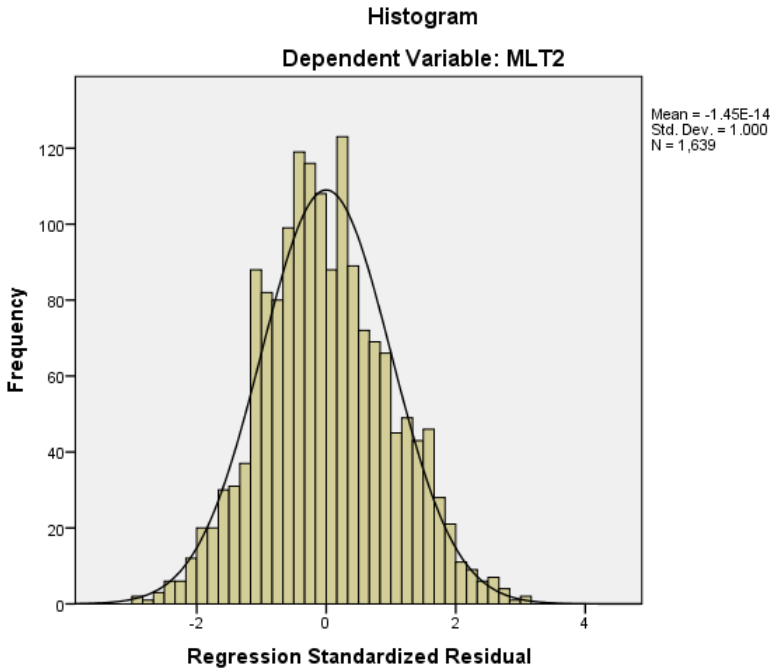

Figure 3.17: Histogram of MLT2 residuals and frequency

The unbiasedness, efficiency and consistency of the variables was thus established. The ANOVA of regression output for MLT2 is summarized in Table 3.2.

Samples (N)	Min	Max	Mean	Mean Absolute Deviation (MAD)	Sum of Squares (Corrected Total)	Sum of Squares (Residuals)	Coefficient of Determination (R^2)
1639	1.184	2.769	1.564	0.130	64.452	38.234	0.407

Table 3.2: ANOVA for MLT2

The R^2 (coefficient of determination) was calculated from sum of squares and was observed to be 0.407. The obtained correlation was:

$$MLT2 = 6.47 - 0.029 \times GR - 11.851 \times \Phi - 1.25 \times 10^{-5} \times GR^2 + 8.674 \times \Phi^2 + 0.037 \times \Phi \times GR, \quad (7)$$

Post-regression, a graphical method was used for comparative analysis of the predicted and the observed data to test the correlation. The graphical method utilized a scatter-plot of experimental and predicted viscosity (Figure 3.18). Ideally, values should be on the unit slope i.e. 45° line and the reliability of the correlation decreases with increasing deviation from the 45° line.

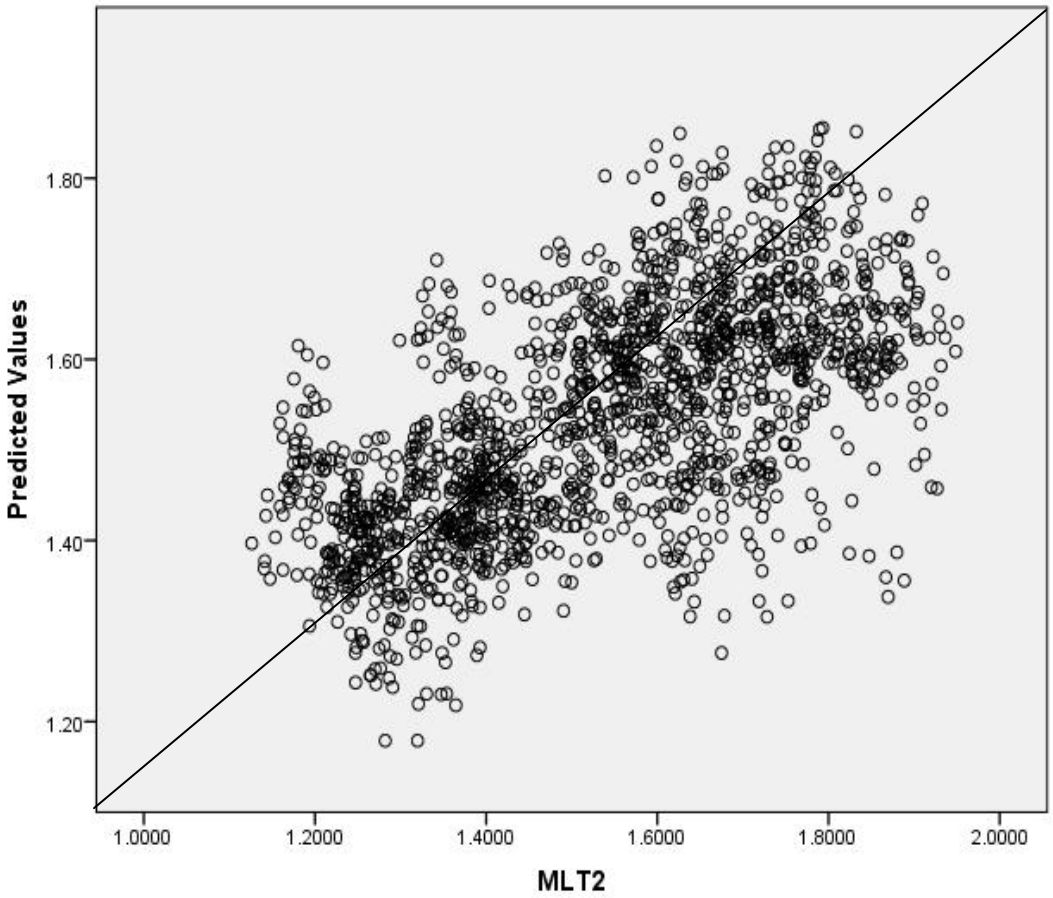

Figure 3.18: MLT2- predicted and expected value crossplot

3.8.2 Regression for SD:

Similar to the procedure for MLT2, it was established from analysis that homoscedasticity was maintained i.e. there existed homogeneity of variance. Multicollinearity was assessed (tolerance= 1.0) and it was seen that the independent variables weren't highly inter-correlated. Normal distribution of data was confirmed from a histogram of residuals as seen in Figure 3.19.

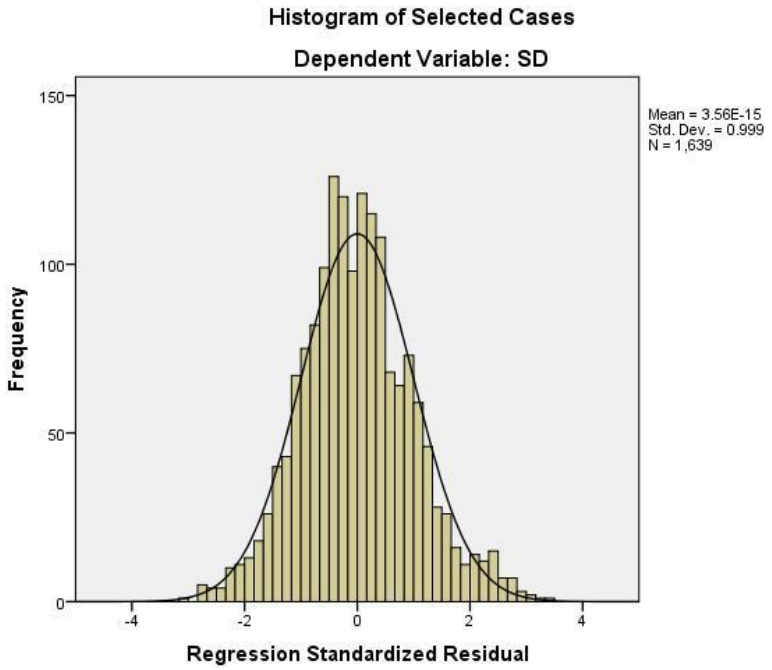

Figure 3.19: Histogram of SD residuals and frequency

The unbiasedness, efficiency and consistency of the variables was thus established. The ANOVA of regression output for SD is summarized in Table 3.3.

Samples (N)	Min	Max	Mean	Mean Absolute Deviation (MAD)	Sum of Squares (Corrected Total)	Sum of Squares (Residuals)	Coefficient of Determination (R^2)
1639	0.437	1.115	0.941	0.058	13.096	7.681	0.413

Table 3.3: ANOVA for SD

The R2 (coefficient of determination) was calculated from sum of squares and was observed to be 0.413. The obtained correlation was:

$$SD = -0.743 + 0.003 \times GR + 5.258 \times \Phi - 3.494 \times 10^{-5} \times GR^2 - 4.736 \times \Phi^2 + 0.008 \times \Phi \times GR, \quad (8)$$

Post-regression, a graphical method was used for comparative analysis of the predicted and the observed data to test the correlation. The graphical method utilized a scatter-plot of experimental and predicted viscosity (Figure 3.20). Ideally, values should be on the unit slope i.e. 45° line and the reliability of the correlation decreases with increasing deviation from the 45° line.

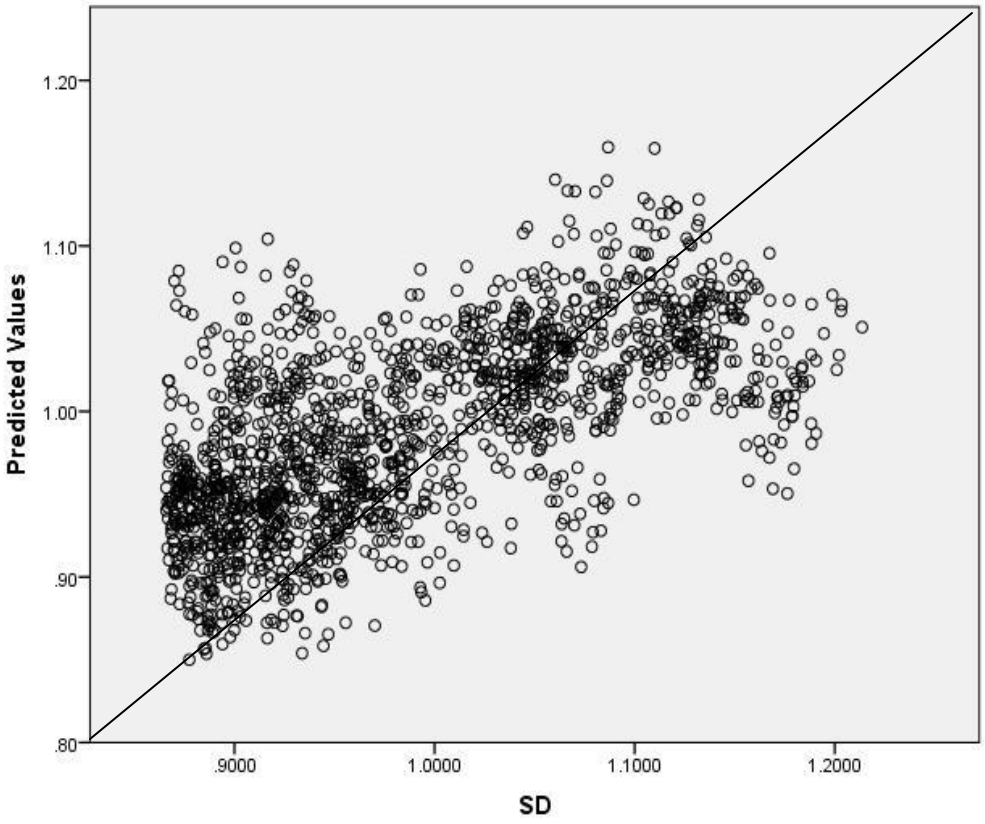

Figure 3.20: SD- Predicted and expected value crossplot

The results obtained were superimposed with the MLT2 and SD logs and the results are displayed in Figure 3.21.

The cross-plots show that the predictions from regression are satisfactory with a tolerable distribution about the unit-slope line. This is further confirmed from the low sum of squares obtained by convergence during regression and the values of coefficient of determination. Hence, the correlations can be used for prediction of synthetic relaxation time distributions in similar formations.

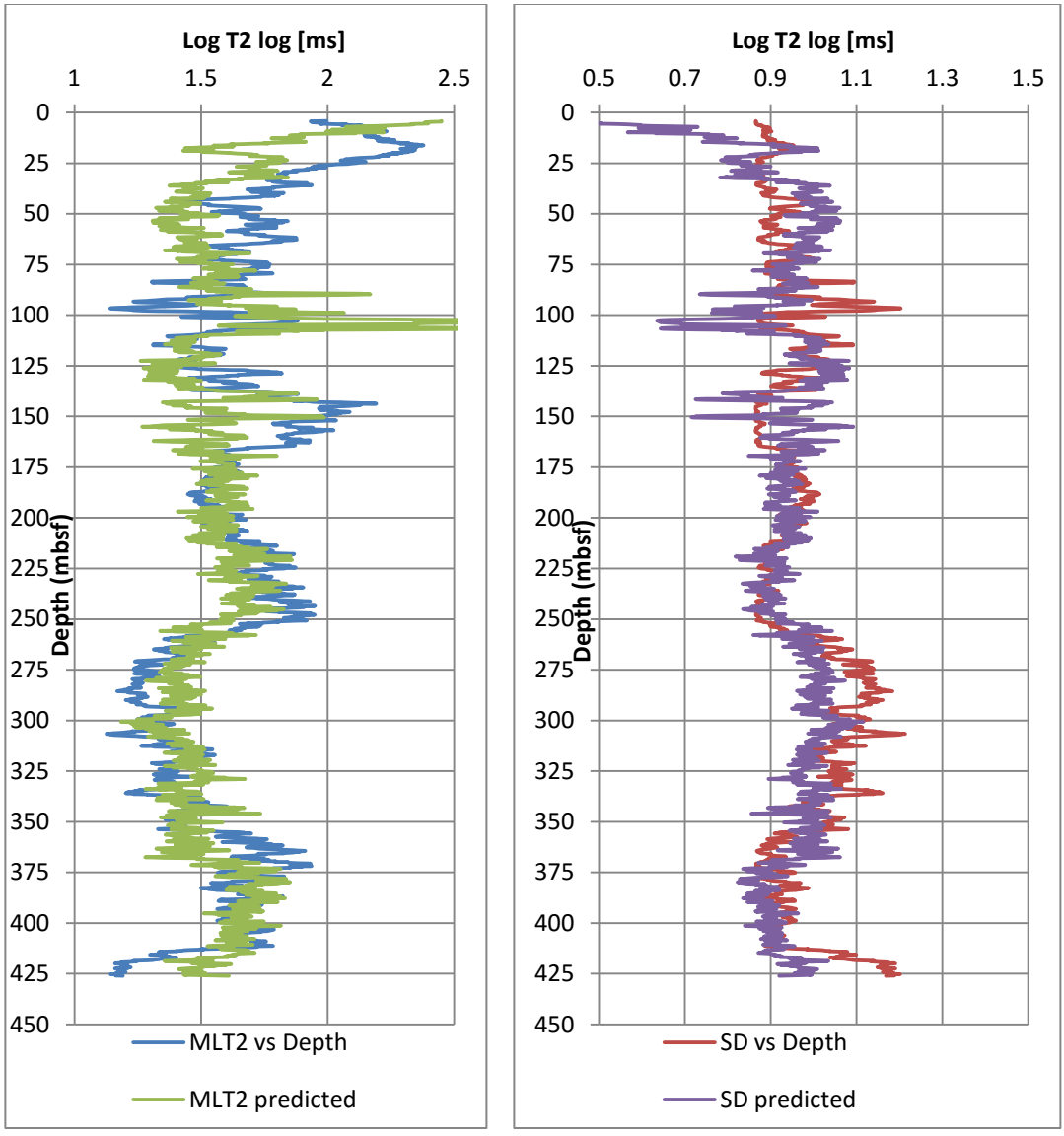

Figure 3.21: KC-151-2 Predicted and actual logs

3.9 MERCURY INJECTION CAPILLARY PRESSURE

We performed mercury injection capillary pressure (MICP) measurements on a sample from a depth of 259.7 mbsf in KC 151-3. The MICP measurement was repeated to test repeatability. MICP is a measurement of the volume of mercury (Hg) that can possibly invade the rock volume. Since mercury does not wet the rock surface, the mercury pressure measured is the capillary pressure (Brown, 2015). The capillary

pressure is useful in calculating the pore throat diameter with certain assumptions. It is a quick and cost-effective method to assess the capillary pressure. It is able to rapidly quantify a sample's interconnected pore system as well as the size distribution of the pore apertures affecting the non-wetting phase saturations and the fluid flow (Shafer and Neasham, 2000). The pressure and pore throat sizes are related by the Washburn equation assuming cylindrical pores:

$$Pc = 2\,\sigma \cos\theta / r \ , \tag{9}$$

where Pc is Capillary Pressure (Pa),

r is pore throat radius (m),

σ is surface tension (0.485 N/m),

θ is contact angle (140°).

The fluid (mercury) enters the pores on application of external pressure which is inversely related to the pore radius.

It is important to note that MICP does not measure all pore throats, but only the pore-throat size to which mercury has access. The MICP curve is a plot of mercury saturation as a function of injection pressure. A pore throat diameter distribution curve may be obtained from these data.

The MICP test progressively measures and records mercury intrusion for each pressure step. The mercury sequentially fills (conforms or closes around) any sample irregularities such as microfractures and is recorded as the mercury intrusion (Shafer and Neasham, 2000). At a finite higher pressure, it finally intrudes the largest pore throat which controls the sample pore volume. This pressure where actual mercury entry begins is called the initial entry pressure. As a result, the intrusion points measured prior to this entry pressure are removed. It is termed as closure/conformance correction. Figures 3.22 and 3.23 show the MICP data for the KC 151-3 sample. In Figure 3.22, conformance pressure manifests as an inflection point at a pressure of 988 psi corresponding to a saturation of 0.139 for mercury. It is subtracted from the total and saturation is

recalculated. The largest pore-throat is measured at this point and is calculated to be 108.97 nm (Equation 9). This correlates with clay sediments.

Figure 3.23 shows the incremental intrusion versus pore radius for both tests run on the sample from KC 151-3. It represents the pore size distribution versus frequency for both samples.

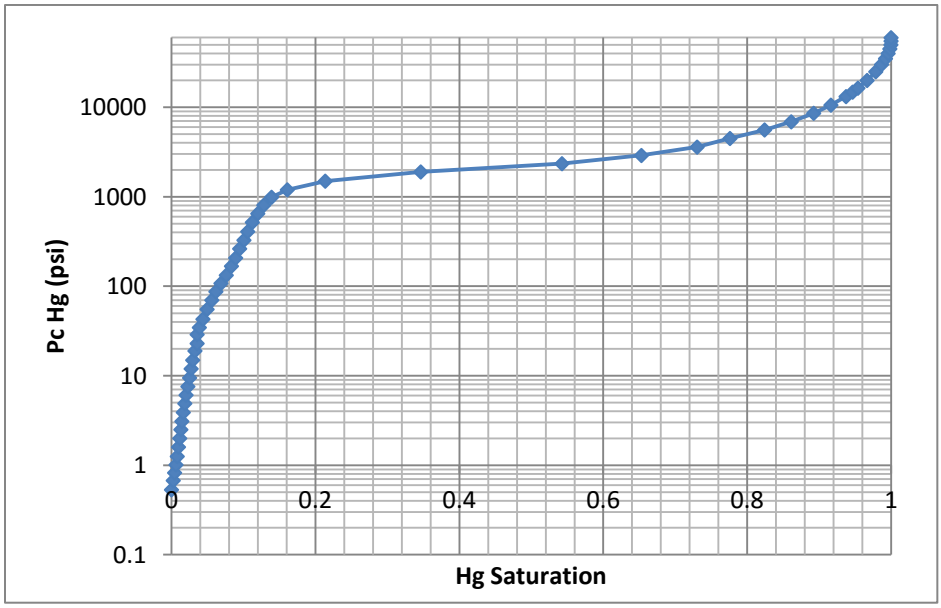

Figure 3.22: Capillary pressure curve

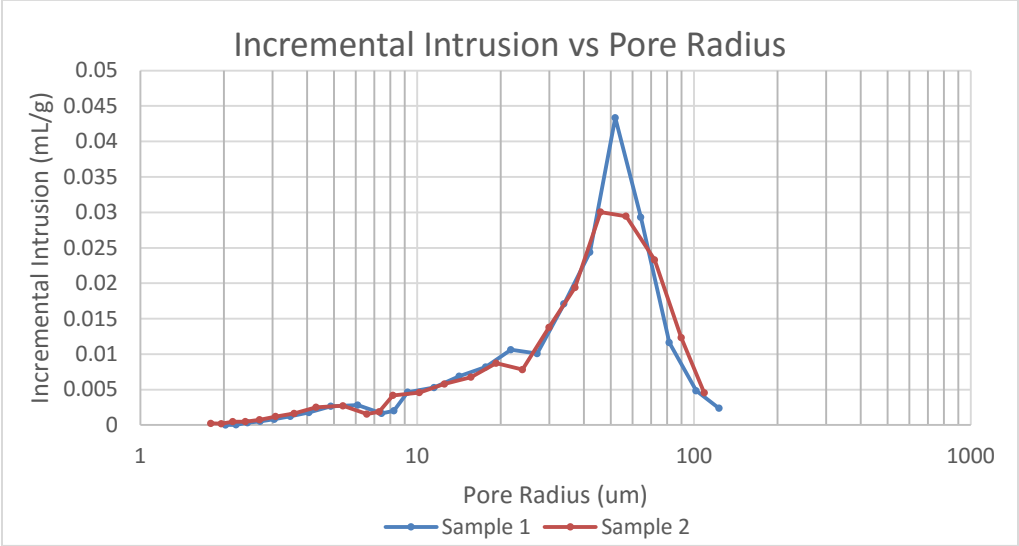

Figure 3.23: Pore radius distribution

3.10 NUCLEAR MAGNETIC RESONANCE AND PORE SIZE DISTRIBUTION

Nuclear Magnetic Resonance or NMR measurements have been a useful tool for analysis of the microscopic structure of porous media. The relation is strongly based on the effect that the rock structure has on promoting proton relaxation (Coates et al., 1999).

The relaxation behavior of a fluid confined inside a pore is affected by both the pore size as well as geometry and gives useful data when an appropriate mathematical method is utilized to model the pore-size distribution.

Proton NMR measures the net magnetization of the hydrogen atoms when an external magnetic field is present (Sulucarnain et al., 2012). The time constant T_2 affects the components of nuclear spin magnetization perpendicular to the magnetic field externally applied.

Since the transverse relaxation time T_2 is dependent on the decay of the spin-echo-train, the larger pores take a larger time to decay and hence reflect a larger relaxation time. This in turn indicates a larger pore size distribution (Coates et al., 1999).

According to Coates et al. (1999), the transverse relaxation time T_2 is affected by three processes: bulk relaxation of the pore fluid, surface relaxation on the pore wall, and relaxation due to diffusion in local magnetic field gradients.

Hence, the equation obtained is of the form:

$$\frac{1}{T_2} = \frac{1}{T_{2bulk}} + \frac{S}{V}\frac{\lambda}{T_{2surface}} + \frac{1}{3}(\gamma\tau B)^2 D \quad , \tag{10}$$

where $\frac{S}{V}$ is pore surface area to volume ratio,

λ is thickness of the surface monolayer,

τ is pulse spacing (pulse-to-echo delay),

γ is gyromagnetic ratio for protons,

D is diffusion coefficient.

In water-bearing sediments, the first and last terms on the right side are small and can usually be neglected which transforms the equation into:

$$\frac{1}{T_2} = \rho_2 \frac{S}{V}, \tag{11}$$

where ρ_2 is termed as surface relaxivity and is dependent on the lithology of the porous medium and interaction of the fluid with the surface.

NMR relaxation measured is the volume-to-surface ratio measured. $\frac{V}{S}$ has dimensions of length and is equivalent to a pore size. As the T_2 is dependent on the pore size, in a water-bearing zone the T_2 distribution is equivalent to the pore size distribution. The ratio while not pore size or diameter depends significantly on the pore shape. It is maximum for spherical surface.

Assuming a cylindrical pore geometry:

Volume $\mathrm{V} = \pi \mathrm{r}^2 \mathrm{h}$, (12)

Surface Area (Curved) $\mathrm{A} = 2\pi \mathrm{rh}$, (13)

Therefore, $\frac{V}{S} = \frac{r}{2}$, (14)

On substitution, pore size distribution can be predicted by the formula:

$$r = 2\,\rho_2 T_2 \ , \quad (15)$$

which gives $r = 2\,\rho_2 10^{MLT2}$. (16)

3.11 COMPARISON OF CLAY PORE SIZE DISTRIBUTION FROM MICP AND NMR

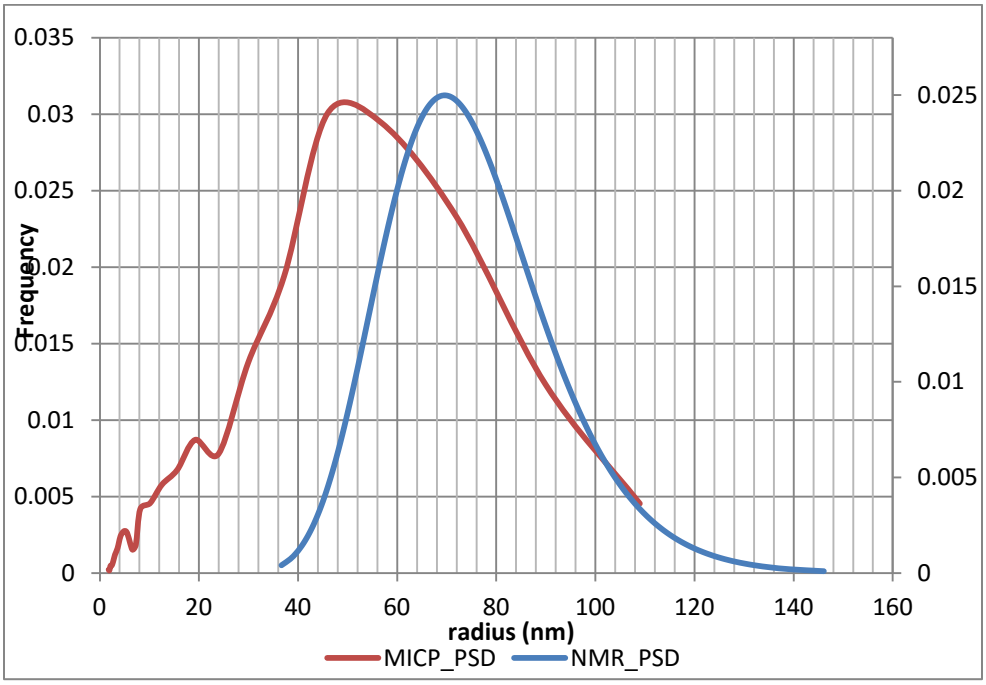

Figure 3.24: Pore size distribution comparison

Figure 3.24 shows a comparative plot of pore size distribution for clays at Keathley Canyon from NMR and MICP. The MICP data is observed to truncate at a maximum pore radius of 108.97 nm after conformance corrections. The maximum pore radius for the NMR curve is defined as the sum of value of the geometric mean and two positive standard deviations about the mean. A synthetic pore size distribution for NMR has been generated in a way that the maximum pore radii coincide for both plots. The NMR curve shows that the mean pore size is ~78 nm while the standard deviation is at a value of ~16 nm for the maximum pore radii to match. The procedure of matching NMR and MICP data at the largest pore size, rather than at the modes of the pore size and T_2 distributions, is consistent with percolation theory (Daigle and Johnson, 2015).

The maximum pore radius is considered as the basis for comparison since NMR is sensitive to pore body size, while MICP depends on capillary pressure which is affected by the pore throat radius. As a result while comparing them, there is a slight difference

observed in the pore size distribution corresponding to the difference between pore body and pore throat size.

The surface relaxivity for clays is not known and is calculated by comparing the two curves in the Figure 3.24. For a surface relaxivity of 1.023 μm/s for the marine clays, it was observed that the maximum pore size for both the curves coincides.

3.12 PORE SIZE DISTRIBUTION LOG GENERATION FROM NMR LOG

The relaxation time synthetically generated using the correlations can now be used for calculation of the pore size distribution for Walker Ridge.

Gamma ray log and porosity data is available for wells WR-313-G and WR-313-H at Walker Ridge. Calculations performed for WR-313-H are shown below. Using the generated correlations (Equations 7 and 8), MLT2 and SD for the well are calculated for all depths. The synthetic logs constructed for relaxation time distribution are shown in Figure 3.25.

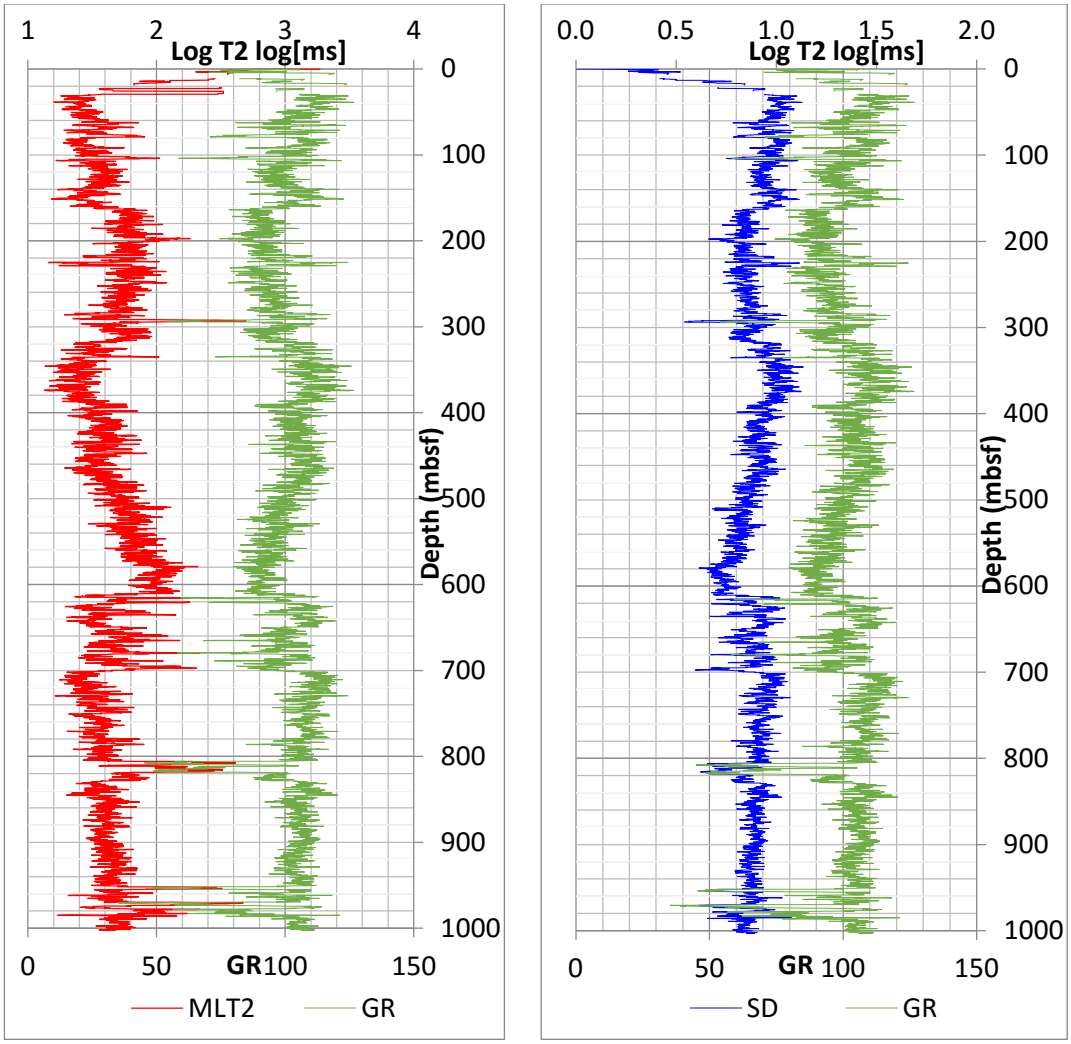

Figure 3.25: Predicted relaxation time distribution for WR-313-H

As discussed earlier, the surface relaxivity is dependent on the lithology of the medium. In absence of measurements for sand, the surface relaxivity value for sands is assumed to be about 16 μm/s (Marschall et al., 1995) and the relaxivity for clays was calculated earlier (1.023 μm/s). Using Equation 16 and values of surface relaxivity for sand and clays, the relaxation time data can be converted to pore size distribution.

A cutoff of GR = 70 GAPI was used for separating the depths into two different formations of sand and clay. All depths having GR values above 70 GAPI are treated as clay for the transformation and below 70 GAPI are assumed to be sand. The pore size distributions generated after the process are shown in Figure 3.26.

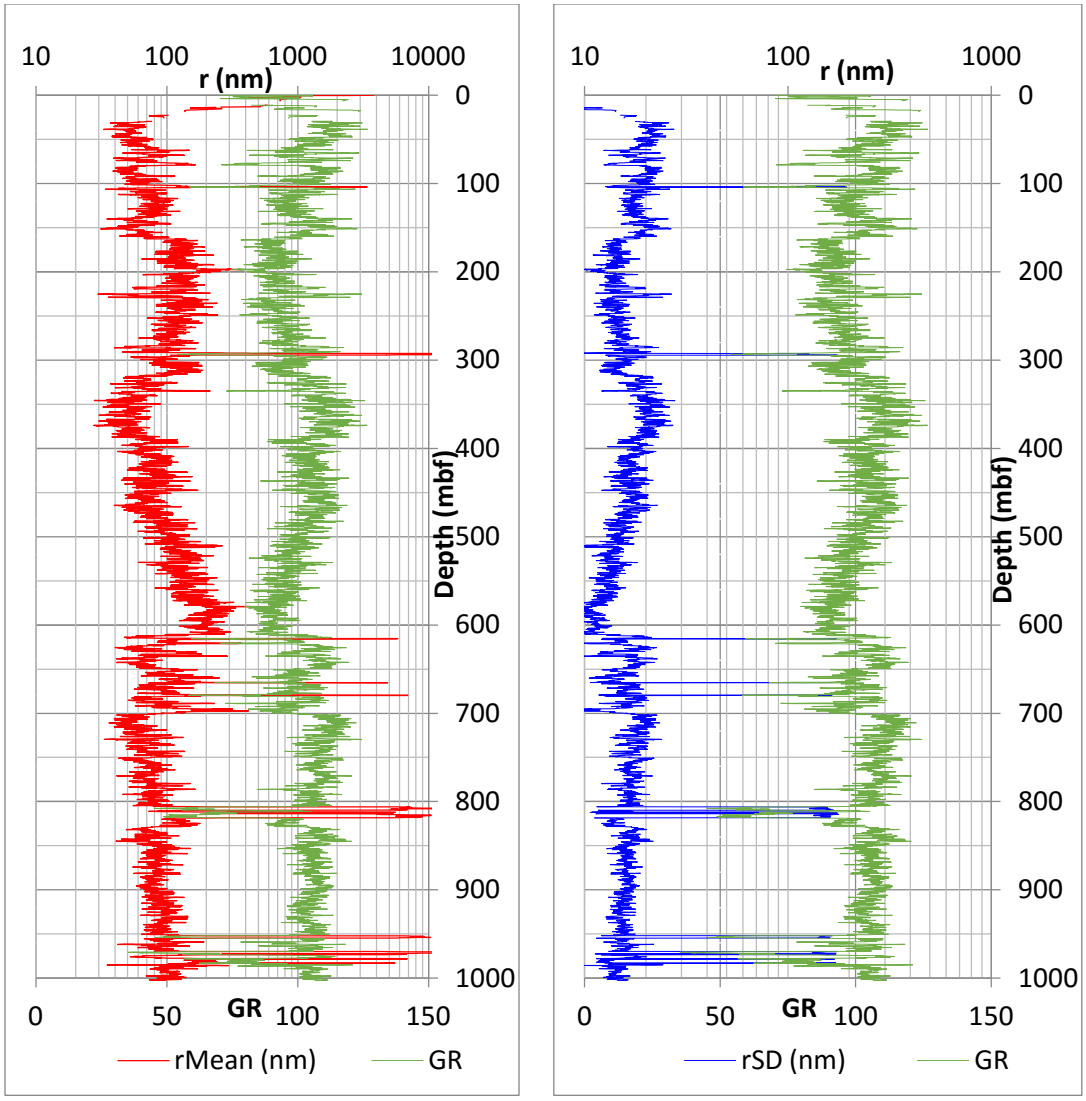

Figure 3.26: Predicted pore size distribution for WR-313-H

The logs in Figure 3.26 indicate that in the clays, the mean pore size is about 170 nm with a standard deviation of 0.865 log-cycles (equivalent to 15 nm). For sands, the data showed that the mean pore size is about 9750 nm and standard deviation of about 0.5917 log-cycles (equivalent to 125 nm).

Similar calculations were also done for the well WR-313-G. More details about the stratigraphy and lithology of the wells at Walker Ridge are discussed in the next chapter.

Chapter 4: Methane equilibrium conditions at Walker Ridge

4.1 IMPORTANCE OF THREE-PHASE ZONE:

As discussed in the previous chapter, the Orange sand at WR-313-H contains hydrates but moving towards WR-313-G, the sand dips below the BGHS in the inter-well region and no hydrate is observed in the sand at WR-313-G (Boswell et al., 2012). The BGHS is usually indicated by the BSR in seismic data. However, the BSR is interpreted to record the top of the gas and not necessarily the base of hydrate occurrence.

Analysis of the seismic signal at the BSR by Chapman et al. (2002) indicated that the base of the hydrate and top of gas do not always coincide but at times create a transition zone. A similar transition zone was reported at ODP sites 889/890 at the Cascadia margin (McKay et al., 1994). Liu and Flemings (2011) describe such as zone as resulting from a broad pore size distribution that will smear the seismic signature between hydrate and free gas by coexistence of multiple phases called a three-phase zone in a discrete range of depths. The thickness of the three-phase zone is dependent on the water depth, methane availability, pore size distribution and occupation of larger pores by different phases.

The distribution of the hydrate and gas inside the sediment column is described by two pressure-temperature dependent equilibrium curves (Liu and Flemings, 2006):

i) The liquid-hydrate (L+H) methane solubility curve, which describes hydrate in equilibrium with the methane dissolved inside the water in the absence of gas.

ii) The liquid-gas (L+G) methane solubility curve, which describes gas in equilibrium with the methane dissolved inside the water in the absence of hydrate.

The methane solubility refers to the concentration of methane (solute) present in the overall mass of water (solvent) in the system under consideration.

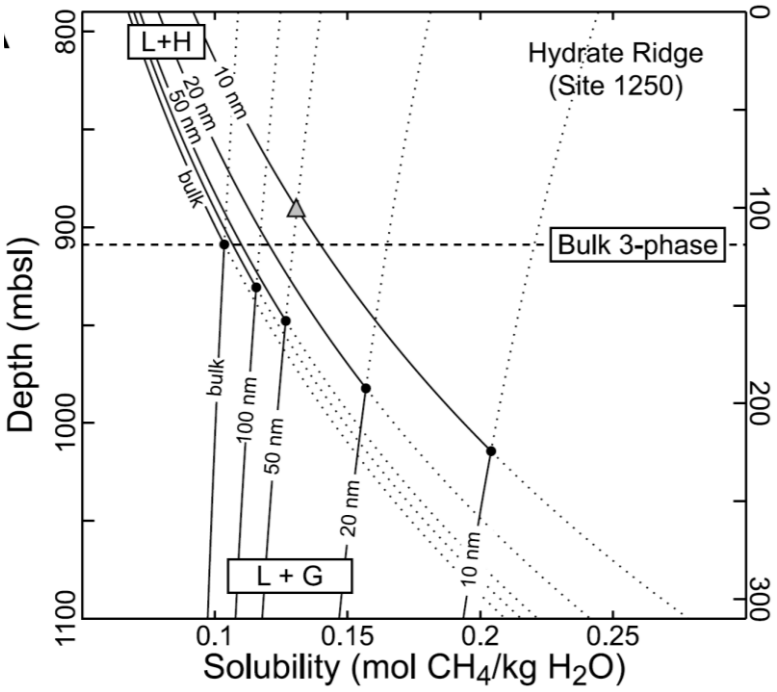

Figure 4.1: L+G and L+H equilibrium curves at Hydrate Ridge for different pore sizes (Liu and Flemings, 2011)

The L+H solubility increases with depth and rising temperature but decreases slightly with increasing pressure. The L+G solubility decreases with increasing temperature and increases with increasing pressure. As seen in Figure 4.1, in marine sediments the net result is that the L+H solubility increases with depth while the L+G solubility decreases with depth. The intersection of the two equilibrium curves is the depth of bulk three-phase stability (Liu and Flemings, 2011). However, as described below, a pore size distribution introduces a thermodynamic degree of freedom into the system whereby instead of a single depth of three-phase equilibrium, the hydrate and gas occupy pores of different sizes to create a region of three-phase equilibrium over a depth range. This occurs due to capillary effects and the additional Gibbs free energy required to create a solid hydrate crystal with finite curvature.

4.2 CAPILLARY EFFECTS IN SEDIMENT PORES:

Methane exists in marine sediments as a gas phase, a dissolved phase in water, or hydrate. The coexistence of immiscible phases (gas or hydrate + water) gives rise to capillary effects (Clennell et al., 1999). Since it is generally assumed that water is the wetting phase in marine sediments, the gas or the hydrate becomes the non-wetting phase. A capillary pressure is created due to the phase pressure difference between the pore water and the hydrate or gas since the interface between the immiscible phases forms a curved surface inside the pore. The hydrate or gas has a higher phase pressure than the water.

Assuming a spherical pore of radius r containing gas or hydrate in which water is the wetting phase, the capillary pressure will be given by:

For gas-water system:

$$P_{cgw} = \frac{-2\sigma_{gw}\, cos\theta_{gw}}{r} \tag{17}$$

For hydrate-water system:

$$P_{chw} = \frac{-2\sigma_{hw}\, cos\theta_{hw}}{r} \tag{18}$$

where σ_{gw} is the gas-water interfacial energy (0.072 J/m2) (Henry et al., 1999),

σ_{hw} is the hydrate-water interfacial energy (0.027 J/m2) (Henry et al., 1999),

θ_{gw} is the gas-water contact angle (180°) (Henry et al., 1999),

θ_{hw} is the hydrate-water contact angle (180°) (Henry et al., 1999).

Effects of capillary pressure on hydrate stability have been extensively studied (Anderson et al., 2003; Uchida et al., 2004). Various statistical thermodynamic models for studying the effects of pore size have also been constructed (Clennell et al., 1999; Henry et al., 1999). Hydrate distribution in layered porous media and capillary effects were investigated using fluid flow models by Malinverno (2010) and Daigle and Dugan (2011).

Water activity is a function of the energy state of the water in the system. On phase change from liquid to solid, the Gibbs free energy of the hydrate phase increases. This increases the solubility of the solid in the liquid, depresses the freezing point of the

solid and is termed the Gibbs-Thomson effect (Daigle and Dugan, 2011). For constant values of pressure and temperature, this causes an increase in the methane solubility and the hydrate growth in smaller pores is inhibited. Conversely, excess energy is also required to create a gas phase in the pores due to the curved gas-water interface involved. The phenomenon demanding excess gas component in the solution for free gas formation in pores is termed capillary supersaturation (Liu and Flemings, 2011). This study considers the capillary effects of both hydrate and gas phases.

Liu and Flemings (2011) calculated the phase fractions of hydrate and gas in and out of the three-phase zone and emphasized the effect of water depth on the capillary inhibition of hydrate stability. This was seen due to the difference between depth of BSR and theoretical base of the GHSZ in deepwater sites.

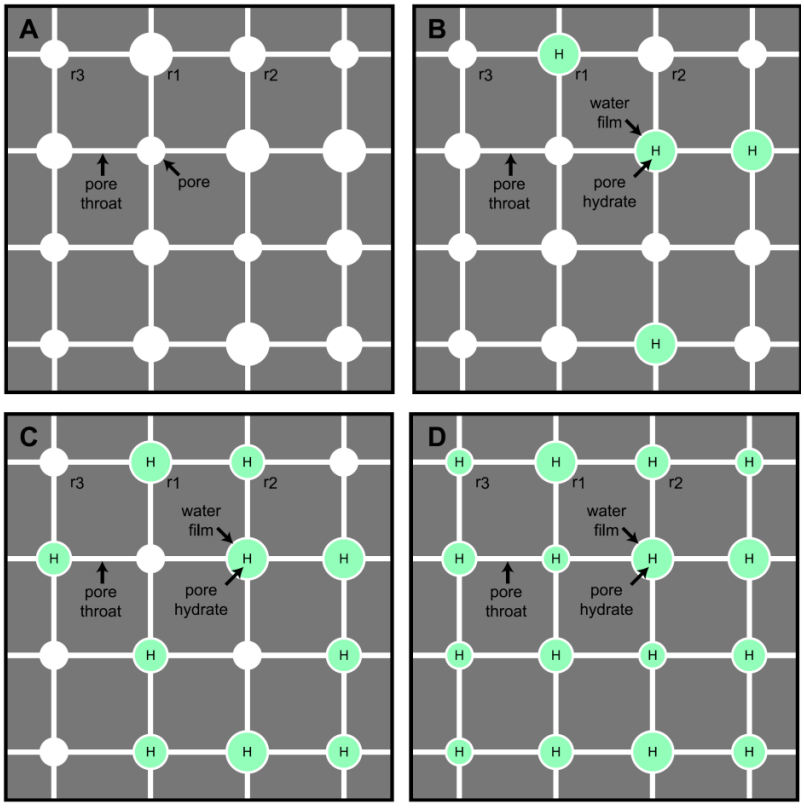

Figure 4.2: Hydrate deposition in spherical pores (Liu and Flemings, 2011). See text for discussion.

As seen in Figure 4.2A, in a porous sediment made of spheres of various radii (r_1>r_2) the smallest supersaturation of methane is necessary to form hydrate in the largest pore (r_1) which happens in Figure 4.2B. Hydrate formation in smaller pores (r_2) is inhibited by redissolution and coalescence in larger pores (r_1) first due to the larger supersaturation required in them. Since the hydrates are precipitated inside the liquid water, which is the wetting phase, the liquid serves as a diffusion pathway for dissolved methane from hydrate to remaining solution. An equilibrium is reached when the hydrates are formed in all the largest pore (r_1) with uniform methane concentration throughout the system. In Figure 4.2C, for further hydrate precipitation in the smaller pores (r_2), greater supersaturation with more methane supply is necessary. The system again achieves equilibrium after hydrate formation in all pores of second-largest radius (r_2). In Figure 4.2D, the methane solubility needed for hydrate precipitation increases as the hydrate grows progressively inside the smaller pores.

Considering the capillary effects on both gas and hydrate, both prefer to be present in separate pores for thermodynamic stability. While water prefers to form a continuous film on the pore surface, the gas and hydrate are both convex to the water. If all three-phases are co-existing, it leads to three interfaces: gas-water, hydrate-water and hydrate-gas. The capillary balance is described by the following equation (Defay et al., 1966).

$$\sigma_{hg} = \sigma_{gw} + \sigma_{hw} , \tag{19}$$

where σ_{hg} is the hydrate-gas interfacial energy. As a result, the hydrate and gas phases prefer to occupy different sized pores to avoid the higher energy interface between gas and hydrate. The capillary forces can cause few pores to be gas saturated and few to be hydrate saturated (Clennell et al., 1999). At three-phase equilibrium, L+H solubility, which is calculated from the smallest hydrate-filling pore, is equal to the L+G solubility, which is calculated from the smallest gas-filling pore.

During coexistence of the three methane phases, there are two non-wetting phases (gas and hydrate). The capillary pressure curves for P_{cgw} and P_{chw} are functions of the phase saturations (S_g and S_h) as well as the distributions of hydrate and gas in pores.

The equilibrium solubilities C_{L+G} and C_{L+H} can be calculated since they are functions of pressure, temperature, salinity and pore size. The smallest hydrate and gas filling pores (r_h and r_g) establish the L+H and L+G solubilities in a distribution of pore sizes. The detailed thermodynamic calculations, done in a manner similar to Liu and Flemings (2011), are described below.

4.3 THERMODYNAMIC CALCULATIONS:

As shown in the Figure 4.3, either hydrate (H) or gas (G) occupies the larger pores and water (L) occupies the smaller pores. At the top of the three-phase zone, gas exists in the largest pore (r_m) whereas the hydrate fills pores down to size r_h^{L+H}. On the other hand, at the base of the three-phase zone, the hydrate exists only in the largest pore (r_m) while the gas fills the pores down to size r_g^{L+G}.

In presence of only two phases, at the top of the three-phase zone (where Liquid + Hydrate are the stable phases) or bottom of the three-phase zone (where Liquid + Gas are the stable phases) the radius r_g or r_h depend only on the phase saturations.

$P_{cgw}(S_g)$ and $P_{chw}(S_h)$ can be used to calculate r_g and r_h, and with increasing saturations these radii become smaller. The top and base of the three-phase zone can be computed using the L+G and L+H solubility curves at the pore sizes (r_m, r_g^{L+G}, r_h^{L+H}). r_m is maximum pore size present in the sediment, r_g^{L+G} denotes the smallest gas-filling pore at L+G equilibrium, and r_h^{L+H} denotes the smallest hydrate-filling pore at L+H equilibrium.

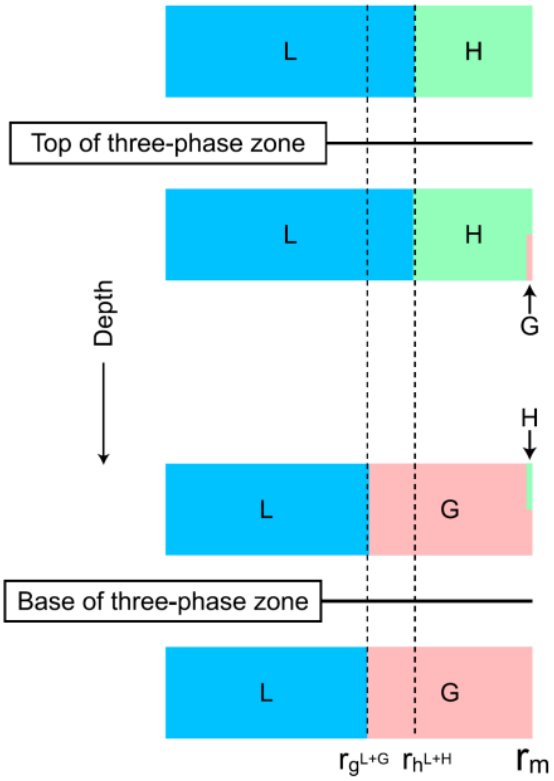

Figure 4.3 Three-phase zone thickness (Liu and Flemings, 2011)

At the top of the three-phase zone, $S_g = 0$; By solving $P_{cgw}(0)$ and $P_{chw}(S_h)$ we get $r_g = r_m$ and $r_h = r_h^{L+H}$. The first gas appears in the largest pore r_m when hydrate fills the pores down to the radius r_h^{L+H}. At the base of the three-phase zone, $S_h = 0$; By solving $P_{cgw}(S_g)$ and $P_{chw}(0)$ we get $r_g = r_g^{L+G}$ and $r_h = r_m$. The last hydrate disappears in the largest pore r_m.

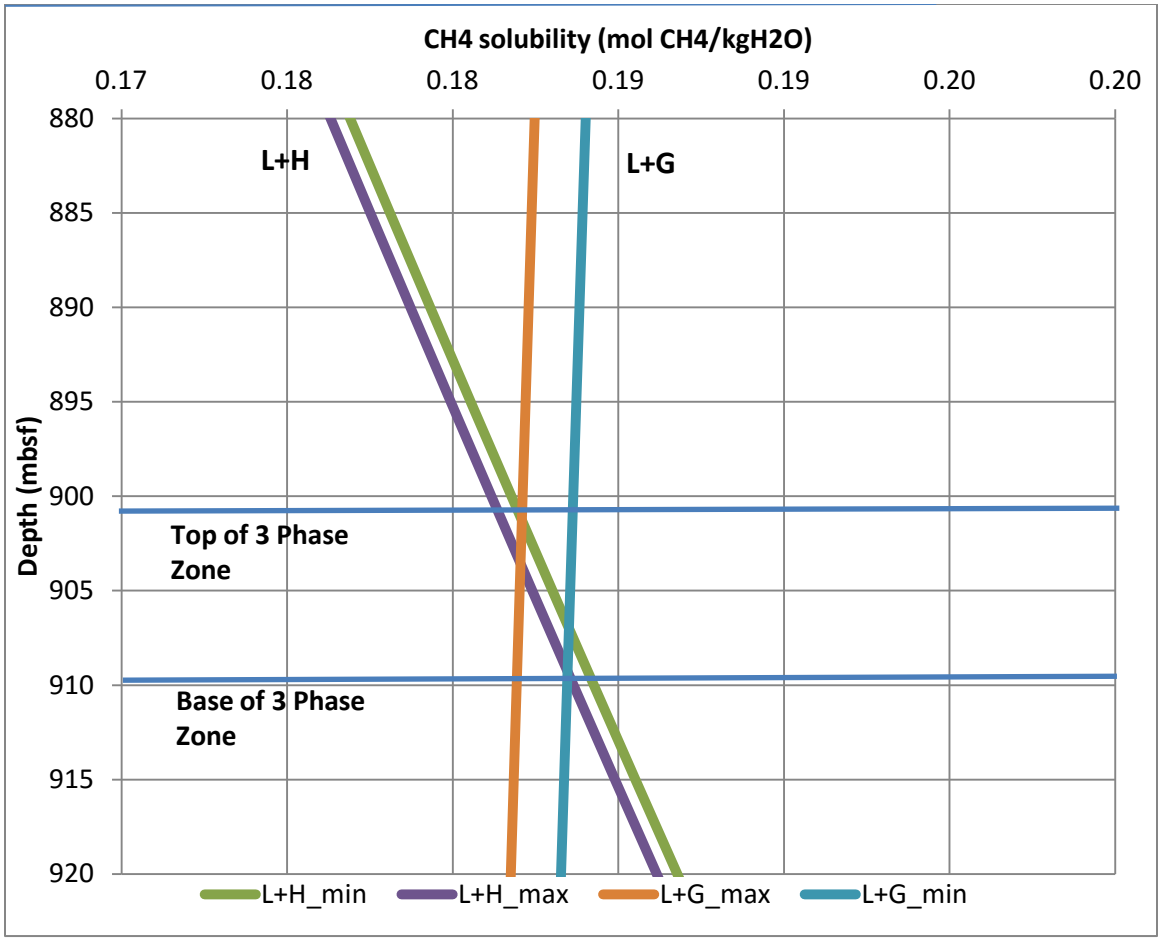

Figure 4.4: Example of three-phase zone

As an example, in Figure 4.4, the top of the three-phase zone is calculated by the intersection of the L+G solubility curve in r_m with the L+H solubility curve in r_h^{L+H}. The base of the three-phase zone is determined by intersection of the L+H solubility curve in r_m with the L+G solubility curve in r_g^{L+G}. The sequence of calculations done for Walker Ridge are elaborated on in the following sections.

4.3.1 L+G equilibrium calculations:

Equilibrium calculations for the L+G curve were conducted according to the model developed by Duan et al. (1992). The model is based on Pitzer (1973) phenomenology for liquid phase and is a highly accurate equation of state developed for

the vapor phase. It can accurately predict the methane solubility in the presence of methane gas in systems like seawater or geothermal brines for temperatures ranging from 9 to 250 °C and 0 to 1600 bar.

The chemical potential of methane in the liquid phase is described by an interaction model from solubility data. At equilibrium, the chemical potentials in liquid (in terms of activity) and gas phase (in terms of fugacity) are given by:

$$\ln \frac{x_{CH4} P}{m_{CH4}} = \frac{\mu_{CH4}{}^{l(0)}(T,P) - \mu_{CH4}{}^{v(0)}(T)}{RT} - \ln \Phi_{CH4}(T,P,x) + \ln \gamma_{CH4}(T,P,m), \quad (20)$$

where m is molality in the liquid phase,

x is composition in vapor phase,

μ is chemical potential,

R is universal gas constant (8.314 J/mol-K),

Φ is fugacity coefficient,

γ is activity coefficient,

v is vapour,

l is liquid,

(0) is standard state.

$\mu_{CH4}{}^{l(0)}$ is the standard chemical potential of methane in liquid phase (ideal solution of unit molality). $\mu_{CH4}{}^{v(0)}$ is the vapor phase standard chemical potential when fugacity is equal to one bar. It is set to zero since the solubility is a function of the difference between $\mu_{CH4}{}^{v(0)}$ and $\mu_{CH4}{}^{l(0)}$.

The fugacity coefficient of methane in vapor phase of methane-water mixtures (Φ_{CH4}) is not very different from that of pure methane for lower temperatures due to relatively small water concentrations (Duan et al., 1992). Therefore, the fugacity coefficient can be calculated from equation of state (EOS) for pure methane:

$$\ln \Phi_{CH4} = Z - 1 - \ln Z + \frac{B}{Vr} + \frac{C}{2Vr^2} + \frac{D}{4Vr^4} + \frac{E}{5Vr^5} + G, \quad (21)$$

where $Pr = {P}/{46.41}$,

$Tr = {T}/{190.6}$,

$Vr = {V}/{0.34146}$,

$Z = \frac{Pr\,Vr}{Tr}$,

$B = a_1 + \frac{a_2}{Tr^2} + \frac{a_3}{Tr^3}$,

$C = a_4 + \frac{a_5}{Tr^2} + \frac{a_6}{Tr^3}$,

$D = a_7 + \frac{a_8}{Tr^2} + \frac{a_9}{Tr^3}$,

$E = a_{10} + \frac{a_{11}}{Tr^2} + \frac{a_{12}}{Tr^3}$,

$F = \frac{\alpha}{Tr^3}$,

$G = \frac{F}{2\gamma}\left[\beta + 1 - \left(\beta + 1 + \frac{\gamma}{Vr^2}\right)\exp\left(-\frac{\gamma}{Vr^2}\right)\right]$.

The values of EOS parameters used to evaluate above variables are given in Table 4.1.

Parameter	Value
a1	8.726E-02
a2	-7.526E-01
a3	3.754E-01
a4	1.073E-02
a5	5.496E-03
a6	-1.848E-02
a7	3.190E-04
a8	2.111E-04
a9	2.017E-05
a10	-1.656E-05
a11	1.196E-04
a12	-1.081E-04
α	4.483E-02
β	7.540E-01
γ	7.717E-02

Table 4.1: EOS parameters (Duan et al., 1992)

Assuming that the water vapour pressure is not affected by presence of NaCl and methane, x_{CH4} can be approximately calculated by:

$$x_{CH4} = (P - P_{H2O})/P, \quad (22)$$

where P_{H2O} is the pure water pressure.

ln γ_{CH4} is derived from a virial expansion of excess Gibbs Energy (Pitzer, 1973).

$$\ln \gamma_{CH4} = \sum_c 2\lambda_{CH4-c}\, m_c + \sum_a 2\lambda_{CH4-a}\, m_a + \sum_c \sum_a \zeta_{CH4-c-a}\, m_c m_a \,, \quad (23)$$

where ζ and λ are interaction parameters.

Substituting equation 23 in equation 20 gives the equation:

$$\ln \frac{x_{CH4} P}{m_{CH4}} =$$

$$\mu CH4l0\ RT - \ln \Phi CH4 + c2\lambda CH4{-}cmc{+}a2\lambda CH4{-}ama{+}ca\zeta CH4{-}c{-}amcma \,, \quad (24)$$

Since all the activity coefficients and the unitless standard chemical potential are functions of pressure and temperature, following the approach by Pitzer (1973), an equation was selected for parameterization.

$$\text{par}\,(T, P) = c_1 + c_2 T + {}^{c_3}/_{T} + c_4 T^2 + {}^{c_5}/_{(680 - T)} + c_6 P + c_7 P \ln T + {}^{c_8 P}/_{T} +$$

$${}^{c_9 P}/_{(680 - T)} + {}^{c_{10} P^2}/_{T} \,, \quad (25)$$

For calculation of the methane solubility at given temperature, pressure and salt composition the activity coefficients and chemical potential need to be evaluated. This was done by Duan et al., (1992) by fitting the least squares fitting of experimental solubility data in aqueous NaCl solutions for a range of temperatures and pressures. The resulting parameters are given in Table 4.2.

T-P coefficient	$\frac{\mu_{CH4}{}^{l(0)}}{RT}$	λ_{CH4-Na}	$\zeta_{CH4-Na-Cl}$
c1	4.303E+01	9.922E-02	-6.239E-03
c2	-6.833E-02	2.579E-05	0.0
c3	-5.687E+03	0.0	0.0
c4	3.566E-05	0.0	0.0
c5	-5.791E+01	0.0	0.0
c6	6.116E-03	0.0	0.0
c7	-7.855E-04	0.0	0.0
c8	-9.425E-02	1.835E-02	0.0
c9	1.921E-02	0.0	0.0
c10	-9.172E-06	-8.072E-06	0.0

Table 4.2: Calculated interaction parameters (Duan et al., 1992)

The ternary interaction parameters (ζ) are only important in high salt concentrations which apart from NaCl usually does not occur in natural sea-water. So neglecting the other interaction parameters (ζ) and minor components, the equation for methane solubility in liquid phase is given by:

$$\ln m_{CH4} = \ln x_{CH4}\, \Phi_{CH4} P - \frac{\mu_{CH4}{}^{o(l)}}{RT} - 2\lambda_{CH4,Na}(m_{Na}) + 0.00624\, m_{Na} m_{Cl}\,, \qquad (26)$$

where $m_{Na} = 0.469$ mol/kg (Holland, 1978),

$m_{Cl} = 0.546$ mol/kg (Holland, 1978).

This equation was therefore applied to all depths at Walker Ridge (WR-313-H and WR-313-G). The L+H equilibrium curve was accordingly plotted for bulk conditions.

4.3.2 L+G equilibrium calculations:

Davie et al. (2004) presented a method of predicting methane hydrate solubility in marine settings at given water depths, seafloor temperature and geothermal gradient. The

pressure and temperature conditions at base of the GHSZ are found by intersection of local pressure and temperature conditions with experimentally determined three-phase equilibrium between the three methane phases of hydrate, free gas and gas in water. The model predicts methane solubility at the base of the GHSZ and subsequently uses simple parametric models to extend the solubility into the GHSZ

Since in marine settings under hydrostatic pressure, the pressure is defined by the water depth and temperature by the seafloor temperature and geothermal gradient, the three-phase temperature can be calculated using empirical formulae or experimental results (Sloan, 1990).

The solubility at the three-phase temperature is given by a linear function of pressure and temperature:

$$C_3(T,P) = C_3(T_0,P_0) + \frac{\partial C_3}{\partial T}(T - T_0) + \frac{\partial C_3}{\partial P}(P - P_0) \quad , \tag{27}$$

where $C_3(T_0,P_0)$ is solubility (mM) at reference temperature T_0 and pressure P_0. At temperature T_0 = 292 K and pressure P_0 = 20 MPa, $C_3(T_0,P_0)$ =156.36 mM. From experimental fitting:

$\frac{\partial C_3}{\partial T}$ = 6.34 mM/K and $\frac{\partial C_3}{\partial P}$ = 1.11 mM/MPa

The solubility can be further accurately represented within the HSZ as an exponential function of temperature by the equation:

$$C_{eq}(T) = C_3(T_3,P)e^{\left(\frac{T-T_3}{\alpha}\right)} \quad , \tag{28}$$

where α = 14.4 °C (From fitting to theoretical values).

The influence of salt on the hydrate-water equilibrium conditions are described by the following equation:

$$C_3(T,P,S) = (1 - \beta S)C_3(T_3,P,0) \, , \tag{29}$$

where S is salt concentration (0.6 mol),

β = 0.1 mol^{-1} (constant).

The calculations for the L+G equilibrium curve were done according to the above equations (27, 28 and 29) and the curve was plotted for bulk conditions.

4.3.3 Capillary effects:

Hydrates inside pores have higher chemical potentials and solubilities than those in bulk. The increase in L+H solubility due to capillary effects can be quantified by the Gibbs-Thomson equation (Clennell et al., 1999):

$$\frac{\Delta C_{L+H}}{C_{L+H0}} = \frac{\Delta\mu}{RT} = \frac{-2\sigma_{hw}\, cos\theta_{hw}}{r}\frac{nV_{\beta}}{RT}\,, \tag{30}$$

where R is the universal gas constant,

T is temperature (K),

$\Delta\mu$ is increase in chemical potential,

n is the stoichiometric factor,

V_{β} is molar volume of water in hydrate lattice,

C_{L+H} is the methane solubility in hydrate equilibrium,

C_{L+H0} is the methane solubility in bulk conditions.

The capillary force due to the curved hydrate-liquid interface increases the supersaturation with decreased pore size. Supersaturation is also required for formation of gas bubbles inside pores. Henry's law shows that gas solubility is directly proportional to the gas pressure ($P_g = P_w + P_{cgw}$).

According to Liu and Flemings (2011), the increase in L+G solubility due to capillary effects is given by:

$$\frac{\Delta C_{L+G}}{C_{L+G0}} = \frac{P_{\mathrm{cgw}}}{P_{\mathrm{w}}} = \frac{-2\sigma_{gw}\, cos\theta_{gw}}{rP_{\mathrm{w}}}\,, \tag{31}$$

where C_{L+G} is the methane solubility in equilibrium with gas.

For any pore size, the increase of methane solubility for the liquid-gas system (ΔC_{L+G}) is larger than the increase of methane solubility for the liquid-hydrate system (ΔC_{L+H}). As a result, the depth of three-phase equilibrium for any pore size always shifts downwards relative to the bulk conditions, increasing the P-T region of hydrate stability. Where the three phases coexist, capillary effects cause a deeper depth of the three-phase equilibrium for a given pore size.

4.3.4 Determination of radii:

4.3.4.1 Calculation of pore radius at Walker Ridge for clays:

According to Daigle et al., (2015), at Keathley Canyon (KC-151-2) the permeability in clays is around 10^{-17} m^2 and porosity is around 0.4, while at Walker Ridge (WR-313-H) the permeability in clays is around 10^{-18} m^2 and porosity is around 0.32.

The maximum radius after conformance correction observed from MICP data is 108.97 nm. For clays at Walker Ridge in the absence of MICP data, this value of maximum radius can be converted according through the J-function (Leverett, 1941) given by:

$$J\,(S_w) = Pc\,(S_w)\frac{\sqrt{k/\Phi}}{\gamma cos\theta}\,, \tag{32}$$

$$\text{Hence, } \sqrt{\frac{k1}{\Phi 1}} = \sqrt{\frac{k2}{\Phi 2}}\,. \tag{33}$$

By calculations, maximum radius (r_m) at Walker Ridge clays is given as 76.73 ≈ 77 nm.

To calculate the required pore radii for the calculations (r_g^{L+G}, r_h^{L+H}) at Walker Ridge, synthetic capillary pressure curves were constructed using the MICP data from Keathley Canyon.

Initially, the MICP data was converted to gas-water and hydrate-water capillary pressures using the appropriate wetting angle and interfacial energy. For gas-water system, entry pressure P_{ce} = 2.00 MPa. For hydrate-water system, entry pressure P_{ce} = 0.75 MPa.

The synthetic capillary pressure curves were constructed according to the Brooks and Corey (1964) model:

$$P_c = P_{ce}\,(S_w)^{-1/\lambda}\,, \tag{34}$$

where P_{ce} is the capillary entry pressure,

λ is index of pore size distribution.

P_{ce} occurs at the largest pore size in the sediment r_m. λ is a measure of the heterogeneity in the porous medium with a smaller value representing a wider distribution of pore sizes.

Three different values of λ (0.6, 0.8, 1.0) were modeled for both gas-water system and hydrate-water system and the results are shown in Figure 4.5 and 4.6.

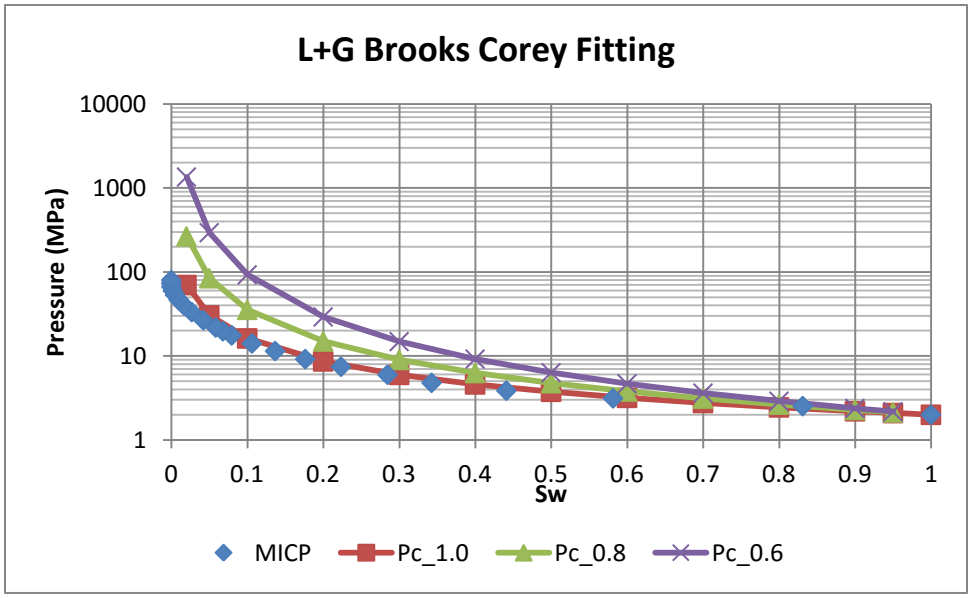

Figure 4.5: L+G Brooks-Corey fitting

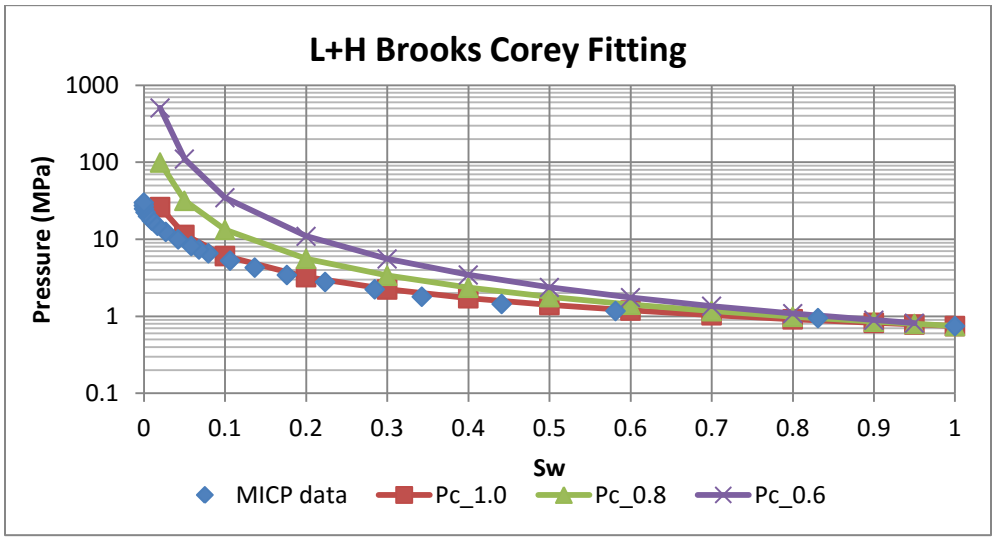

Figure 4.6: L+H Brooks-Corey fitting

As seen in the Figures 4.5 and 4.6, the value of λ= 1.0 gives the best fit. Assuming a gas saturation of 10%, from the Brooks-Corey equation it was seen that P_c = 2.20 MPa. After equivalent conversion to Walker Ridge radius, r_g^{L+G} = 65.41 ≈ 66 nm. From the logs at Walker Ridge, the hydrate saturation in clays is observed to be very low. Assuming hydrate saturation of 5%, From the Brooks-Corey equation, it was seen that the P_c = 0.79 MPa. After equivalent conversion to Walker Ridge radius, r_h^{L+H} = 68.71 ≈ 69 nm.

4.3.4.2 Calculation of pore radius at Walker Ridge for sands:

In absence of MICP and NMR data for sands at Walker Ridge, the maximum and minimum pore radii were calculated from the pore size distributions predicted from relaxation time data conversion.

The mean pore size for sand was inferred from the synthetic logs to be about 9750 nm. The standard deviation (SD) for sand was inferred to be 0.5917 log-cycles. Assuming the Maximum Radius $r_{max} = 2\,\rho_2 10^{(MLT2+2SD)}$ = 10,000 nm. Assuming the Minimum Radius $r_{min} = 2\,\rho_2 10^{(MLT2-2SD)}$ = 9,500 nm. These radii are used for calculating the L+G and L+H equilibrium curves at Walker Ridge.

4.4 PRESSURE-TEMPERATURE CONDITIONS AT WALKER RIDGE:

With assumed variables of pure methane, normal salinities (35 ppt) along with sea floor temperature of 4°C, the equilibrium temperature at BGHS for Walker Ridge where strata intersect the BGHS gives an average geothermal gradient of 19.6 °C/km (McConnell and Kendall, 2002). The water depth is 1985 m below sea level with a hydrostatic gradient of 10.143 kPa/m.

4.5 THREE-PHASE ZONE IN CLAYS:

The curves for three-phase zone in clays have been plotted in the Figure 4.7.

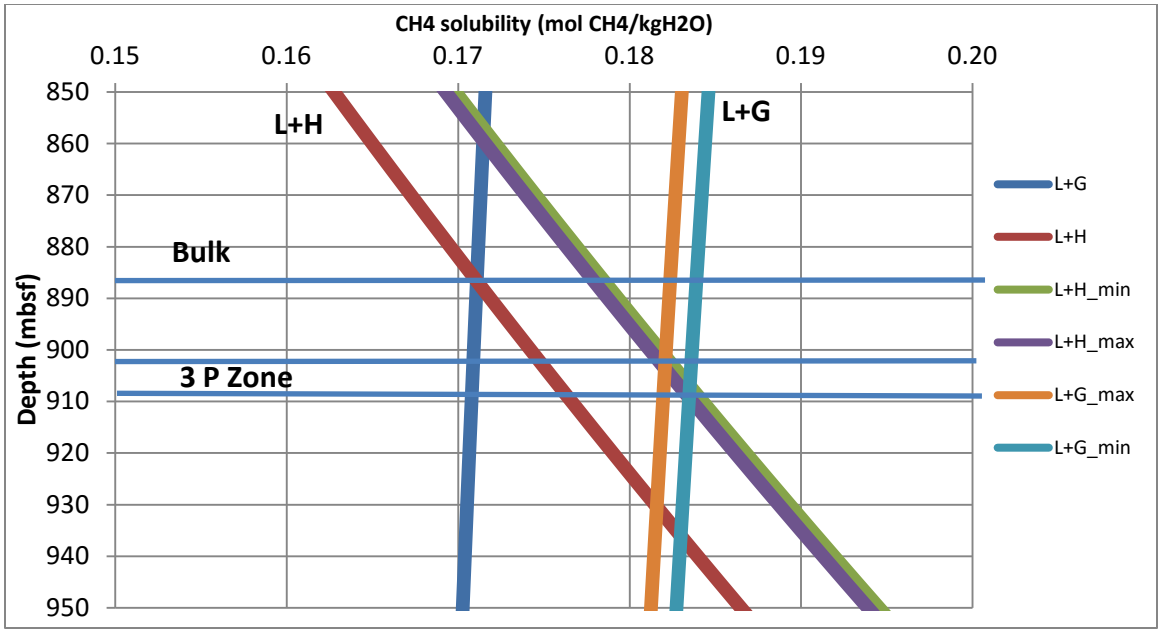

Figure 4.7: Three-phase zone thickness for clays. The curves plotted are L+G (Bulk), L+G_max (r_m) = 77 nm, L+G_min (r_g^{L+G}) = 66 nm, L+H(Bulk), L+H_max (r_m) = 77 nm, L+H_min (r_h^{L+H}) = 69 nm.

The intersection of curves for the bulk-three-phase depth is at 885 mbsf. However, the three-phase zone depth for the actual clay sediments is seen to shift downwards due to capillary effects. The top of the three-phase zone is given by the intersection of the curves L+G_max and L+H_min, and is observed to be at a depth of around 903 mbsf. The base of the three-phase zone is determined by the intersection of the curves L+G_min and L+H_max, and occurs around a depth of 908 mbsf. Thus the thickness of the three-phase zone for clays at WR-313 is estimated to be around 5 m.

4.6 THREE-PHASE ZONE IN SAND:

The curves for three-phase zone in sands are plotted in Figure 4.8.

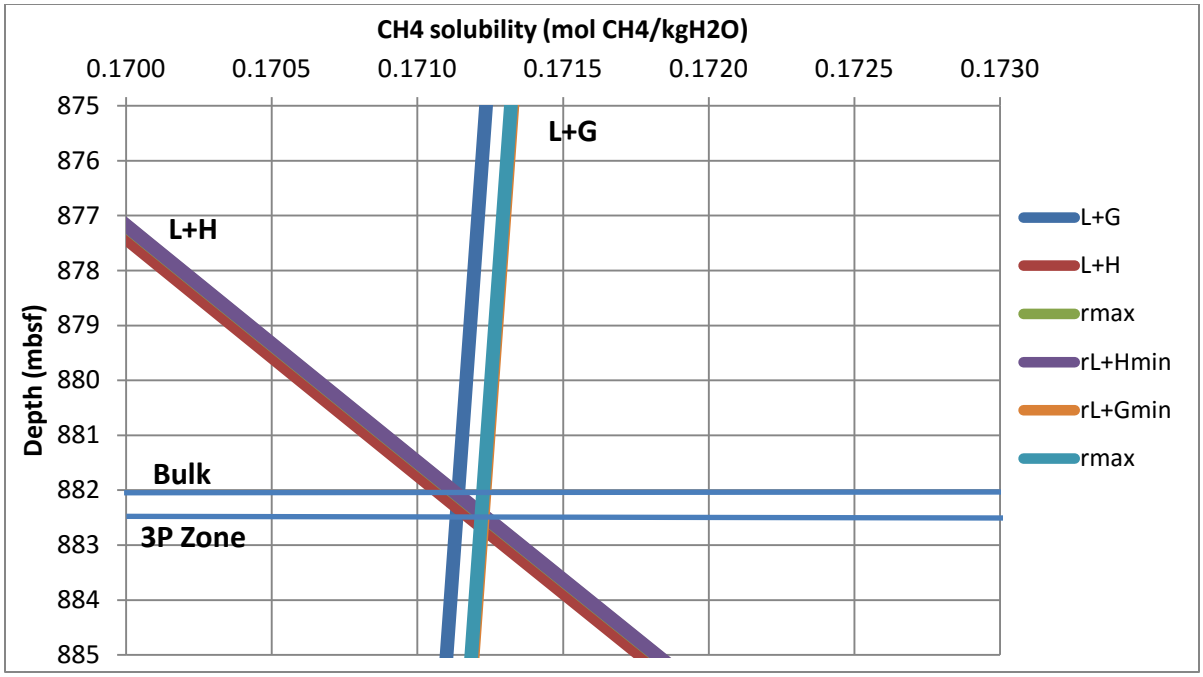

Figure 4.8: Three-phase zone thickness for sands. The curves plotted are (L+G) Bulk, L+G_max (r_m) = 10,000 nm, L+G_min (r_g^{L+G}) = 9,500 nm, (L+H) Bulk, L+H_max (r_m) = 10,000 nm, L+H_min (r_h^{L+H}) = 9,500 nm.

The intersection of curves for the bulk-three-phase depth is at 882 mbsf. However, the three-phase zone depth for the sand sediments is seen to shift downwards only slightly due to capillary effects in the larger pores. The top of the three-phase zone is given by the intersection of the curves L+G_max and L+H_min, and is observed to be at a depth of around 882.5 mbsf. The base of the three-phase zone is determined by the intersection of the curves L+G_min and L+H_max, and occurs around a depth of 882.5 mbsf. The difference between them is very small and the thickness of the three-phase zone for sands at WR-313 is estimated to be in order of few centimeters. The results and their implications are discussed in detail in the next chapter.

Chapter 5: Discussion of results

In this chapter, the significance of the differences in the three-phase zone thickness obtained in the sands and clays at Walker Ridge is discussed. Additionally, the characteristics of the three-phase zone at WR-313 are compared with that of the three-phase zone at Blake Ridge. This chapter also includes the assumptions in the calculations and the future drilling plans.

5.1 WR-313: Discussion of three-phase zone thickness

As seen in the previous chapter the thickness of the three-phase zone is different in sands (< 1 m) and in clays (about 5 m). This difference is a result of the difference in capillary effects in the two sediment types.

The maximum and minimum pore sizes calculated for sands are over two orders of magnitude higher than those considered for clays. The larger pores have weaker capillary effects due to the large pore radii. As a result, the three-phase zone is quite narrow in sediments with larger pores such as sands and is close to the bulk three-phase depth. On the other hand, in clays the capillary effects are more pronounced due to smaller pores. The three-phase zone is relatively thicker than in sands and is significantly shifted below the bulk three-phase depth.

A three-phase zone was observed at another location (Blake Ridge) which is at similar depths as Walker Ridge. The results obtained in this work are compared with the results at Blake Ridge which is a well-studied location also located in similar deep-water marine sediments. This will help us understand if the results for three-phase behaviour obtained at WR-313 are unique or show normal behavior.

5.2 Three-phase zone at Blake Ridge:

Blake Ridge has a water depth of about 2780 m and a geothermal gradient of about 36.9 °C/km. The depth of the bulk three-phase stability is predicted at 481 mbsf.

Capillary pressure curves were obtained for Blake Ridge by Henry et al. (1999). The sample obtained had a smaller nominal pore radius than the samples at other

locations such as Hydrate Ridge since it was more deeply buried. The capillary entry pressure was only about 0.055 MPa with a maximum pore radius (r_m) of about 2620 nm and a mean pore size of about 75 nm. This gives rise to an extremely broad pore size distribution. This may be attributed to presence of high number of diatoms in the sediments (Liu and Flemings, 2011).

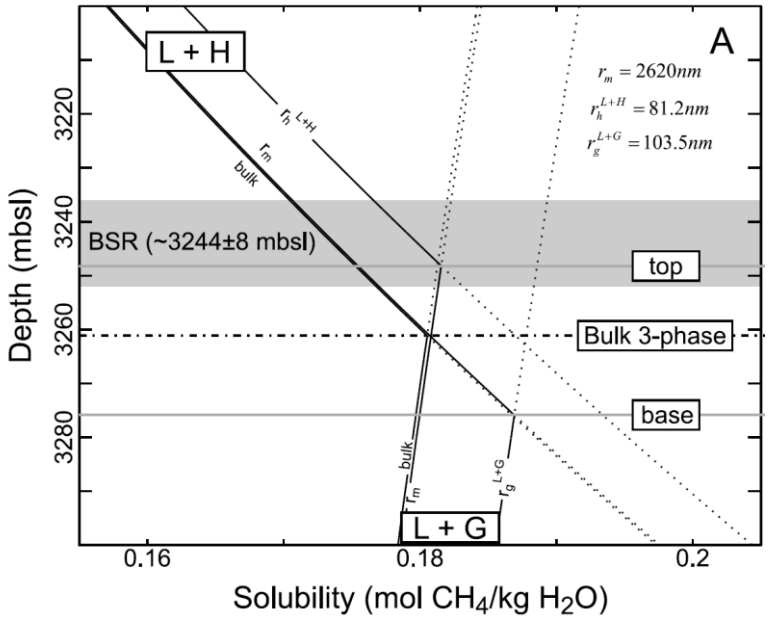

Figure 5.1: Three-phase zone at Blake Ridge (Liu and Flemings, 2011)

As seen in the Figure 5.1, the BSR is estimated to be at 3244 ± 8 mbsl with bulk equilibrium at 3261 mbsl. The broad pore size distribution has given rise to a thick three-phase zone with a gradual transition from hydrate-saturated to gas-saturated sediments. According to the calculations made by Liu and Flemings (2011), the top and base of the three-phase zone as interpreted from the intersection of the equilibrium curves indicated that the top of the three-phase zone is about ~13 m above the depth of the bulk-three-phase equilibrium. The base of the three-phase zone is observed to be about ~14.7 m below the bulk stability depth. Thus, the total thickness of the three-phase zone is estimated to be about 27.7 m.

5.3 COMPARISON OF THREE-PHASE ZONES AT WALKER RIDGE AND BLAKE RIDGE:

The thick three-phase zone at Blake Ridge (27.7 m) passing through the bulk three-phase equilibrium is a result of the capillary effects due to the wide distribution of pores. Most of the hydrate near the top of the three-phase zone (3274 mbsl) is in smaller pores and gas in larger pores. On the other hand, near the base of the-three-phase zone (3246.3 mbsl), most gas exists in the smaller pores allowing stable hydrates in the larger pores. Capillary effects typically shift the depth of three-phase stability downwards with respect to the bulk conditions. However, with a broader pore size distribution, the existence of gas in larger pores can shift the top of the three-phase zone above that predicted by bulk equilibrium. Thus, gas can exist about the bulk conditions allowing hydrate to form below the bulk equilibrium depth.

Meanwhile, at Walker Ridge, in clays the pore size distribution after corrections is extremely narrow with the maximum pore radius (r_m) about 76 nm. This gives rise to a very narrow pore size distribution. The gas and hydrates have a very narrow band of depth for coexistence and as a result the top of the three-phase zone (903 mbsf) is below the bulk equilibrium (885 mbsf). This is in range with the BSR observed around the depth of 900 mbsf at WR-313-H (Frye et al., 2012).

5.4 IMPACT OF THREE-PHASE ZONE ON PHASE REVERSAL OF BSR:

BSRs are either associated with diagenetic boundaries or as indications of gas hydrates. The majority of documented BSRs is related to the negative impedance at the transition from hydrate bearing sediments (higher compressional velocity) to gas bearing sediments (lower compressional velocity) at base hydrate stability zone (BGHS). The BSRs therefore have a reflection polarity opposite to that of the seafloor. At times, the top of gas occurs below the BGHS causing an offset between the BSR and BGHS which can be an indication for a possible three-phase zone.

According to Shedd et al. (2012), most commonly observed BSRs are 'discontinuous' in the sense that they reflect areas where a variable lithology exists consisting of alternating sediments of fine and relatively coarse grains. The BSR is observed only in the coarse grained sediments.

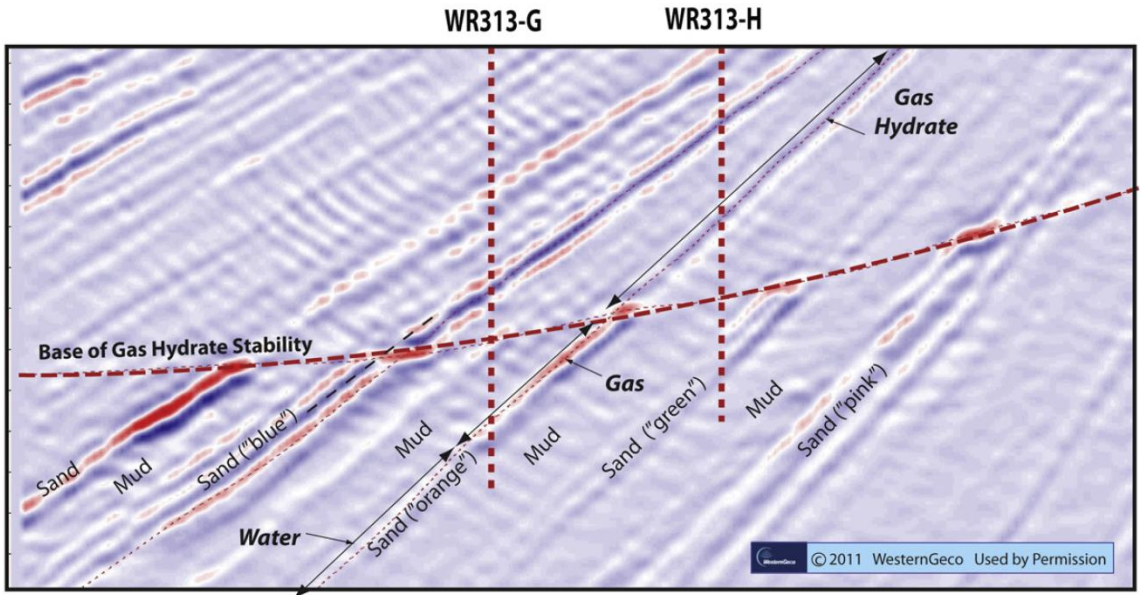

Figure 5.2: BSR phase reversal at WR-313 (Boswell et al., 2012)

Similar behavior was observed at Walker Ridge as shown in the Figure 5.2. The phase reversal behavior is more pronounced in sands than clays whereby the BSR is observed clearly in sands but not in clays.

Although other factors may influence the presence or absence of a BSR, there exists a possibility that the thicker three-phase zone observed in clays (~5 m) causes a diffuse front for the acoustic impedance contrast. Alternatively, the thinner three-phase zone in sand (<1 m) serves as a sharp impedance contrast. As a result the BSR is only observed in the sand layers at Walker Ridge.

5.5 Assumptions in Three-Phase Zone Calculations

The values of thickness and depth of the three-phase zone observed at Walker Ridge are a result of a series of complex calculations with a number of assumptions made during the modeling process.

In absence of MICP and NMR data being readily available at Walker Ridge, pore size distributions had to be synthetically generated by correlation with Keathley Canyon.

Transformations of pore sizes were made from Keathley Canyon to Walker Ridge assuming uniform porosity and permeability throughout the particular type of sediments. Availability of more data from future coring will eliminate the need of these assumptions and will reduce the uncertainty regarding the exact depths of the three-phase zones in both sands as well as clays.

The lithology has been classified into two distinct units: sands and clays with uniform characteristics. The pore sizes will be affected as a result of lithology and compaction. Compaction reduces the pore size and affects the methane equilibrium. While the relative homogeneity of sediments will reduce the deviation from results, the varying properties of sediments will affect the phase behavior.

Additionally, during the thermodynamic calculations the pores were assumed to be of a uniform shape with constant mean curvature. The actual formation geometry is highly irregular with varying pore size and shapes throughout the depths of investigation. The capillary behavior assumptions are according to hydrate formation behavior and may not be valid for hydrate dissociation due to hysteresis behavior not accounted for in the calculations.

The mineral surface is assumed to be hydrophilic and the contact angles are assumed to be 180°, similar to Liu and Flemings (2011). The actual minerals will have inclusions which will reduce the contact angles and affect the calculations.

Overall, the assumptions made during the calculation process are reasonable but availability of additional petrophysical and thermodynamic data will improve the results and reduce the uncertainty.

5.6 FUTURE DRILLING AT WR-313

Drilling of more wells at Walker Ridge in the Terrebonne Basin has been planned under the DOE Project 'Deepwater Methane Hydrate Characterization and Scientific Assessment' (DE- FE0023919).

The objectives of the project are to gain insight into the nature, formation, occurrence, and physical properties of methane hydrate-bearing sediments for methane

hydrate resource appraisal through the planning and conduct of drilling, coring, logging, testing, and analytical activities to assess the geologic occurrence, regional context, and characteristics of marine methane hydrate deposits in the Gulf of Mexico (GOM) and/or other areas of the U.S. Outer Continental Shelf.

A number of sites have been selected for drilling at Walker Ridge and will include pressure coring. The pressurized cores will provide detailed data for characterization of hydrates and the formation.

Chapter 6: Conclusion and future work

This work was able to predict the thickness and the depth of the three-phase zone at Walker Ridge in both sand and clay sediments in addition to generation of synthetic pore size distribution.

The study has shown that, for a narrow pore size distribution in clays in higher depth sediments, the top of the three-phase zone may exist below the bulk equilibrium depth which in contrast with previous studies such as at Walker Ridge by Liu and Flemings (2011). This needs to be further analyzed after more number of wells are drilled and more pore size data is available at WR-313.

The top of the three-phase zone will affect the depth where the hydrate saturation starts decreasing (competition with gas for pore space), which will affect the amount of hydrate in place. While 80% of hydrates in Terrebonne basin are believed to be in fractured-clay rich intervals, the other 20% (about 4.409 billion cubic meters) are estimated to be inside Pleistocene age sand units discussed in this work. Although the ultimate recoverable reserves are uncertain, there is a high potential for their extraction in the future (Frye et al., 2012). The depth and thickness of the three-phase zone is therefore an important factor for estimating the hydrate resources.

Another important observation is the possible explanation of discontinuous BSR presence being due to the different sediment lithologies encountered at the BGHS. The differing three-phase zone thickness affects the acoustic impedance contrast at the interface which in turn affects the strength of the reflected signal (Shedd et al., 2012). Other locations with different lithologies present at the BGHS should be similarly studied for signs of discontinuous BSR.

Studying the gas hydrate in-place resources at WR-313 in Terrebonne Basin also gives an indication of the gas production potential. Field tests have shown that hydrates can be produced from sandstone reservoirs by completion and production methods used for conventional hydrocarbons (Collett et al., 2009). The simulations have shown potentially high rates of gas production largely as a result of relatively deep burial as well

as interbedded units which allows more sources of heat flux which will oppose the expected endothermic cooling during dissociation (Myshakin et al., 2012).

Myshakin et al (2012) also simulated a number of cases for gas production using the depressurization method at constant bottom-hole pressure. The hydrate deposits were observed to be readily produced due to the high intrinsic reservoir-quality and their proximity to the base of hydrate stability. Thus, analysis of hydrate stability conditions serves as an important precursor before hydrate production can be initiated in the future from deepwater marine deposits such as those found at Walker Ridge-313.

To conclude, studying the stability conditions of gas hydrates is an important step towards estimation of the amount of gas in hydrate resources in place, allowing the prediction of temperature at the base of observed gas hydrate stability zone (Liu and Flemings, 2011), detecting the presence of a discontinuous BSR as well as for determination of feasibility for natural gas extraction from a gas hydrate field.

Bibliography

Anderson, R., M. Llamedo, B. Tohidi, and R. W. Burgass (2003), Experimental measurement of methane and carbon dioxide clathrate hydrate equilibria in mesoporous silica, *J. Phys. Chem*., 107,3507–3514

Archie, G.E. (1942). "The electrical resistivity log as an aid in determining some reservoir characteristics". *Petroleum Transactions of AIME* 146: 54–62.

Beaudoin, Y. C., Waite, W., Boswell, R. and Dallimore, S. R. (eds), (2014). *Frozen Heat: A UNEP Global Outlook on Methane Gas Hydrates. Volume 1*. United Nations Environment Programme, GRID-Arendal

Beaudoin, Y. C., Dallimore, S. R., and Boswell, R. (eds), (2014). *Frozen Heat: A UNEP Global Outlook on Methane Gas Hydrates. Volume 2*. United Nations Environment Programme, GRID-Arendal

Bily, C. and Dick, J.W.L., (1974). Naturally occurring gas hydrates in the Mackenzie Delta, N.W.T. Bull. *Can. Pet. Geol*., 32: 340-352.

Birchwood, R., and Noeth, S. (2012). Horizontal stress contrast in the shallow marine sediments of the Gulf of Mexico sites Walker Ridge 313 and Atwater Valley 13 and 14 - Geological observations, effects on wellbore stability, and implications for drilling. *Marine and Petroleum Geology*, 34(1), 186–208.

Boswell R., Yamamoto K., Lee S. R., Collett T., Kumar P., Dallimore S., (2014), *Chapter 8 - Methane Hydrates, In Future Energy (Second Edition),* edited by Trevor M. Letcher, Elsevier, Boston, Pages 159-178, ISBN 9780080994246

Boswell, R. and Collett, T.S., (2011). Current perspectives on gas hydrate resources. *Energy and Environmental Science*, 4, 1206-1215

Boswell, R., and T. Collett, (2006). The gas hydrates resource pyramid, *Fire in the Ice*, US Department of Energy, Office of Fossil Energy, National Energy Technology Laboratory, 6(3), p. 5-7.

Boswell, R., Collett, T. S., Frye, M., Shedd, W., McConnell, D. R., and Shelander, D. (2012). Subsurface gas hydrates in the northern Gulf of Mexico. *Marine and Petroleum Geology*, 34(1), 4–30.

Boswell, R., Frye, M., Shelander, D., Shedd, W., McConnell, D. R., and Cook, A. (2012). Architecture of gas-hydrate-bearing sands from Walker Ridge 313, Green Canyon 955, and Alaminos Canyon 21: Northern deepwater Gulf of Mexico. *Marine and Petroleum Geology*, 34(1), 134–149.

Brooks, J.M., Kennicutt II, M.C., Fay, R.R., McDonald, T.J. and Sassen, R., (1984). Thermogenic gas hydrates in the Gulf of Mexico. *Science*, 225: 409-411.

Brooks, R. H., and A. T. Corey (1964), *Hydraulic Properties of Porous Media*, 27 pp., Colorado State Univ., Fort Collins, Colo.

Brown, A. A. (2015). Interpreting Permeability From Mercury Injection Capillary Pressure Data, 41660.

Chapman, N. R., J. F. Gettrust, R. Walia, D. Hannay, G. D. Spence, W. T. Wood, and R. D. Hyndman (2002), High-resolution, deep-towed, multichannel seismic survey of deep-sea gas hydrates off western Canada, *Geophysics*, 67, 1038–1047.

Clennell, M. B., M. Hovland, J. S. Booth, P. Henry, and W. J. Winters (1999), Formation of natural gas hydrates in marine sediments: 1. Conceptual model of gas hydrate growth conditioned by host sediment properties, *J. Geophys. Res*., 104, 22,985–23,003

Coates, G.R. and Xiao, L. and Prammer, M.G.,(1999), *NMR logging: principles and applications, Halliburton Energy Services*

Collett, T. S., A. H. Johnson, C. C. Knapp, and R. Boswell, (2009), Natural Gas Hydrates: A Review, in Natural gas hydrates— Energy resource potential and associated geologic hazards: *AAPG Memoir* 89, p. 146– 219

Collett, T. S., Lee, M. W., Zyrianova, M. V., Mrozewski, S. a., Guerin, G., Cook, A. E., and Goldberg, D. S. (2012). Gulf of Mexico Gas Hydrate Joint Industry Project Leg II logging-while-drilling data acquisition and analysis. *Marine and Petroleum Geology*, 34(1), 41–61.

Collett, T., Riedel, M., Cochran, J., Boswell, R., Kumar, P., Sathe, A., Party, T.N.E.S., (2008). Indian continental margin gas hydrate prospects: results of the Indian National Gas Hydrate Program(NGHP) Expedition 01. In: *Proceedings of the 6th International Conference on Gas Hydrates (ICGH 2008)*, Vancouver, British Columbia, Canada.

Cook, A.E., Goldberg, D., Kleinberg, R.L., (2008). Fracture-controlled gas hydrate systems in the northern Gulf of Mexico. *Marine and Petroleum Geology.* 25, 932–941

Daigle, H., and Dugan, B. (2009). Extending NMR data for permeability estimation in fine-grained sediments. *Marine and Petroleum Geology*, 26(8), 1419–1427.

Daigle, H., and Dugan, B. (2010). Origin and evolution of fracture-hosted methane hydrate deposits. *Journal of Geophysical Research: Solid Earth*, 115(11), 1–21.

Daigle, H., Cook, A., and Malinverno, A. (2015). Permeability and porosity of hydrate-bearing sediments in the northern Gulf of Mexico. *Marine and Petroleum Geology*, 68, 551–564.

Daigle, H., and Johnson, A. (2015). Combining Mercury Intrusion and Nuclear Magnetic Resonance Measurements Using Percolation Theory. *Transport in Porous Media*, 111(3), 669–679

Dallimore S., Wright F., Yamamoto K., Bellefleur G., (2012) Proof of Concept for gas hydrate production using the depressurization technique, as established by the JOGMEC/NRCan/Aurora Mallik 2007-2008 Gas Hydrate production research well program *Geol. Surv. Can. Bull*, 601 , pp. 1–16

Davidson, D.W. (1973). *Clathrate hydrates. In Water: A comprehensive treatise (ed. F. Franks)*. pp. 115-234. Plenum Press, New York

Davidson, D.W., EI-Defrawy, M.K., Fuglem, M.O. and Judge, A.S., (1978). Natural gas hydrates in northern Canada. In: *National Research Council of Canada. Proc. 3rd Int. Conf. on Permafrost,* 1978, 1: 938-943.

Davie, M. K., Zatsepina, O. Y., and Buffett, B. a. (2004). Methane solubility in marine hydrate environments. *Marine Geology*, 203(1-2), 177–184.

Defay, R., Prigogine I., and Bellemans A., (1966), Surface Tension and Adsorption, translated from French by D. H. Everett, Longmans, London

Duan, Z., Moller, N., Greenberg, J., and Weare, J. H. (1992). The prediction of methane solubility in natural waters to high ionic strength from 0 to 250°C and from 0 to 1600 bar. *Geochimica et Cosmochimica Acta*, 56(12), 4303.

Frye, M., (2008). Preliminary Evaluation of In-place Gas Hydrate Resources: Gulf of Mexico Outer Continental Shelf. *Minerals Management Service Report* 2008-004.

Frye, M., Shedd, W., and Boswell, R. (2012). Gas hydrate resource potential in the Terrebonne Basin, Northern Gulf of Mexico. *Marine and Petroleum Geology*, 34(1), 150–168.

Hadley, C., D. Peters, A. Vaughan, (2008). Gumusut-Kakap project: Geohazard characterisation and impact on field development plans, *International Petroleum Technology Conference*,12554, 15 pp.

Hammerschmidt, E.G. (1934). Formation of gas hydrates in natural gas transmission lines. *Ind. Eng. Chem*., 26, No. 8, 851-855

Hancock, S., Collett, T.S., Dallimore, S.R., Satoh, T., Huenges, E., Henninges, J. (2005). Overview of thermal stimulation production test results for the Japex/JNOC/GSC Mallik 5L- 38, *Gas Hydrate Research Well.*

Henry, P., Thomas, M., and Clennell, M. Ben. (1999). Formation of natural gas hydrates in marine sediments: 2. Thermodynamic calculations of stability conditions in porous sediments. *Journal of Geophysical Research*, 104(B10), 23005.

Holland, H. D. (1978) *The Chemistry of the Atmosphere and Oceans*. Wiley Interscience.

Hollister, C. D., Ewing, J. I., Hathaway, J. C., Lancelot, Y., Paulus, F. J., Habib, D., Luterbacher, H. P., Poag, C. W., Wilcoxon J. A., (1972) *DSDP Initial Report Volume XI.* Retrieved from 10.2973/dsdp.proc.11.1972

Hutchinson, D. R., Hart, P. E., Collett, T. S., Edwards, K. M., Twichell, D. C., and Snyder, F. (2008). Geologic framework of the 2005 Keathley Canyon gas hydrate research well, northern Gulf of Mexico. *Marine and Petroleum Geology*, 25(9), 906–918.

Hutchinson, D., Boswell, R., Collett, T., Dai, J. C., Dugan, B., and Frye, M. (2005). Gulf of Mexico Gas Hydrate Joint Industry Project Leg II : Walker Ridge 313 Site Selection. Image *(Rochester, N.Y.),* 1–35.

Johnson, A. (2011). Global resource potential of gas hydrate – a new calculation, *Proceedings of the 7th International Conference on Gas Hydrates (ICGH 2011)*, Edinburgh, Scotland, United Kingdom, July 17-21, 2011.

Kvenvolden K. A., and Barnard L. A., (1983) *DSDP Initial Report Volume LXXVI* Retrieved from 10.2973/dsdp.proc.76.1983

Lee, M. W., and Collett, T. S. (2008). Integrated analysis of well logs and seismic data to estimate gas hydrate concentrations at Keathley Canyon, Gulf of Mexico. *Marine and Petroleum Geology*, 25(9), 924–931.

Lee, M.W., Collett, T.S., (2009). Gas hydrate saturations estimated from fractured reservoir at Site NGHP-01-10, Krishna-Godavari Basin, India. *Journal of Geophysical Research* 114,

Liu, X., and Flemings, P. B. (2006). Passing gas through the hydrate stability zone at southern Hydrate Ridge, offshore Oregon. *Earth and Planetary Science Letters*, 241(1-2), 211–226.

Liu, X., and Flemings, P. B. (2011). Capillary effects on hydrate stability in marine sediments. *Journal of Geophysical Research: Solid Earth*, 116(7), 1–24.

Leverett M.C. (1941). Capillary behaviour in porous solids. *Transactions of the AIME* (142): 159–172

MacKay, M. E., R. D. Jarrard, G. K. Westbrook, and R. D. Hyndman (1994), Origin of bottom-simulating reflectors: Geophysical evidence from the Cascadia accretionary prism, *Geology*, 22,459–462.

Malinverno, A. (2010). Marine gas hydrates in thin sand layers that soak up microbial methane. *Earth and Planetary Science Letters*, 292(3-4), 399–408.

Marschall, D., Gardner, J. S., Mardon, D., and Coates, G. R. (1995). Method for correlating NMR relaxometry and mercury injection data, *Society of Core Analysts*.

McConnell, D., Kendall, B.,(2002). Images of the base of gas hydrate stability, northwest Walker Ridge, Gulf of Mexico. *Offshore Technology Conference, OTC 14103*, 10 pp.

McConnell, D., Zhang, Z., (2005). Using acoustic inversion to image buried gas hydrate distribution. NETL-DOE. *Fire in the Ice*, Fall 2005, pp. 3e5.

Milkov, A.V., Claypool G. E., Lee Y. J., Xu, W., Dickens G.R., Borowski W.S.,(2003) ODP Leg 204 Scientific Party, In situ meth- ane concentrations at Hydrate Ridge, offshore Oregon: new constraints on the global gas hydrate inventory from an active margin, *Geology* 31 (2003) 833–836

Milkov, A.V., G.E. Claypool, Y.-J. Lee, M.E. Torres, W.S. Borowski, H. Tomaru, R. Sassen, P. Long, and the ODP Leg 204 Scientific Party. (2004). Ethane enrichment, propane depletion, and other compositional variations in subsurface gases: A new indicator of gas hydrate occurrence in marine sediments.

Myshakin, E. M., Gaddipati, M., Rose, K., and Anderson, B. J. (2012). Numerical simulations of depressurization-induced gas production from gas hydrate reservoirs at the Walker Ridge 313 site, northern Gulf of Mexico. *Marine and Petroleum Geology*, 34(1), 169–185.

Nehring, R., 1991. Oil and gas resources. In: Salvador, A. (Ed.), The Gulf of Mexico Basin. *The Geology of North America*, vol. J. GSA, Boulder, CO, pp. 445–494.

Peters, E. J. (2012). Advanced Petrophysics. Austin, TX: Live Oak Book Company

Pinkston J. and Stern L. (2010), Gas Hydrates Burning (jpeg). Retrieved from http://gallery.usgs.gov/photos/03_08_2013_fj0Meq5DCw_03_08_2013_1#.VwGXCKQrLIU

Pitzer, K. S. (1973) Thermodynamics of electrolytes: I. Theoretical basis and general equations. *J. Phys. Chem.* 77, 268-217.

Riedel, M., Collett, T.S., Malone, M.J., and the Expedition 311 Scientists, (2006). *Proc. IODP, 311*: Washington, DC (Integrated Ocean Drilling Program Management International, Inc.)

Ripmeester, J.A., Tse, J.A., Ratcliffe, C.I., Powell, B.M.,(1987) A New Clathrate Hydrate Structure Nature, 325,135

Roberts, H., (1995). High resolution surfacial geology of the Louisiana middle-to- upper continental slope. *Trans. Gulf Coast Assoc. Geol. Soc. XLV*, 503–508.

Ruppel, C., (2011), Methane Hydrates and Future of Natural Gas, *MITEI Natural Gas Report,*1-25

Ruppel, C., Boswell, R., and Jones, E. (2008). Scientific results from Gulf of Mexico Gas Hydrates Joint Industry Project Leg 1 drilling: Introduction and overview. *Marine and Petroleum Geology*, 25(9), 819–829.

Ruppel, C., T. Collett, R. Boswell, T. Lorenson, B. Buczkowski, and W. W. (2011), A new global gas hydrate drilling map based on reservoir type, *Fire in the Ice*: Department of Energy, Office of Fossil Energy, National Energy Technology Laboratory, Methane Hydrate News Letter, 11, 13-17

Shafer, J., and Neasham, J. (2000). Mercury Porosimetry Protocol for Rapid Determination of Petrophysical and Reservoir Quality Properties. *International Symposium of the Society of Core Analysts*, 18–22.

Shedd, W., Boswell, R., Frye, M., Godfriaux, P., and Kramer, K. (2012). Occurrence and nature of " bottom simulating reflectors" in the northern Gulf of Mexico. *Marine and Petroleum Geology*, 34(1), 31–40.

Shelander, D., Dai, J. and Bunge, G. (2010). Predicting saturation of gas hydrates using pre-stack seismic data. *Marine Geophysical Researches* 31.

Sloan, E.D. and Koh, C.A. (2007). Clathrate *hydrates of natural gases, third edition*. 721 p. CRC Press, Boca Raton

Sloan, E.D., (1990). *Clathrate Hydrates of Natural Gases*. Marcel Dekker, New York

Sulucarnain, I., Sondergeld, C., and Rai, C. (2012). An NMR Study of Shale Wettability and Effective Surface Relaxivity. *SPE Canadian Unconventional*, (November), 1–11.

Suter, J.R., Berryhill Jr., H.L., (1985). Late quaternary shelf-margin deltas, Northwest Gulf of Mexico. *AAPG Bull.* 69, 77–91

Tréhu, A., Ruppel, C., Holland, M., Dickens, G., Torres, M., Collett, T., Schultheiss, P. (2006). Gas Hydrates in Marine Sediments: Lessons from Scientific Ocean Drilling. *Oceanography*, 19(4), 124–142. h

Uchida, T., S. Takeya, E. M. Chuvilin, R. Ohmura, J.Nagao, V. S.Yakushev, V. A. Istomin, H. Minagawa, T. Ebinuma, and H. Narita (2004), Decom- position of methane hydrates in sand, sandstone, clays, and glass beads, *J. Geophys. Res*., 109

Von Stackelberg, M. and Muller, H.R. (1951). On the structure of gas hydrates. *J. Chem. Phys.*, 19, 1319-1320

Von Stackelberg, M. and Müller, H. R. (1954): "Feste Gashydrate", Z. *für Elektrochemie*, 58, 25

Zheng, J., Ponnivalavan B., Linga P., (2015), Thermodynamics and applications of CO2 hydrates, Reaction Mechanisms in Carbon Dioxide Conversion, *Springerlink*, p373-402